BEHAVIOUR OF REINFORCED CONCRETE SLABS
MADE WITH HIGH STRENGTH CONCRETE

AMGAD AHMED HUSSEIN, B.Sc. (Eng.)

BEHAVIOUR OF REINFORCED CONCRETE SLABS
MADE WITH HIGH-STRENGTH CONCRETE

by

© Amgad Ahmed Hussein, B.Sc. (Eng.)

A thesis submitted to the School of Graduate
Studies in partial fulfillment of the
requirements for the degree of
Master of Engineering

Faculty of Engineering and Applied Science
Memorial University of Newfoundland
August 1990

St. John's　　　　　Newfoundland　　　　Canada

Canadä

ABSTRACT

The present research investigation deals with the structural behaviour of two-way slabs made with high-strength concrete subjected to punching shear.

A high-strength concrete mix, suitable for offshore applications, was developed using conventional cement and aggregates available in Newfoundland. The incorporation of silica fume and high-range water reducing agent made it possible to achieve high strengths at early ages. A compressive strength of 70 MPa at 28 days was achieved for concrete mix incorporating 12 % class F fly ash, 8 % condensed silica fume and a high-range water reducing agent of naphthalene formaldehyde base. The relevant rheological and mechanical properties of the mix were examined. In addition, an experimental program was carried out to study the effect of cold ocean water, simulated under laboratory conditions, on the mechanical properties of green high-strength concrete containing silica fume and fly ash.

Seventeen slabs were tested in the structural laboratory at M.U.N. The effect of the reinforcement ratio, concrete strength, slab depth and column size on the behaviour of the slabs was investigated. The structural behaviour of the tested slabs with regard to deformations, strains, ultimate capacity, and modes of failure was examined. Test results revealed that the present North American Codes are unsafe for high-strength concrete slabs, since they overestimate the influence of the concrete strength, as a factor, on the ultimate capacity of two-way slabs.

Based on the test results, a mechanical model was adopted. The formulation takes into account the actual behaviour of the high-strength concrete and steel. The proposed model gave a fairly good agreement between the predicted and experimental punching loads.

ACKNOWLEDGEMENTS

Contents

iv

List of Figures

ix

List of Tables

List of Symbols

A_s	area of steel
A_{sr}	area of the steel in the radial direction
A_{st}	area of the steel in the tangential direction
E_c	modulus of elasticity of concrete
E_s	modulus of elasticity of steel
F_{cr}	radial concrete force
F_{ct}	tangential concrete force
F_{ctot}	total concrete forces in a radial direction
F_{sr}	radial steel force
F_{st}	tangential steel force
F_{stot}	total steel forces in a radial direction
K	coefficient
P_{code}	ultimate shear capacity
P_{flex}	ultimate flexural load capacity as predicted by yield line
P_{test}	ultimate test load
T	oblique compressive force in the imagenary conical shell assumed by Kinnunen and Nylander
a	side dimension between supports of a square slab
b	perimeter of the loaded area
c	side dimension of a square column
d	slab effective depth
f_{bu}	limiting bearing strength
f'_c	compressive cylinder strength of concrete

xiii

f_{cu}	cube concrete strength
f'_r	modulus of rupture
f'_{sp}	tensile splitting strength of concrete
f_t	concrete tensile strength
f_y	yield strength of reinforcing steel
h	slab overall depth
m	unit moment capacity
m_u	positive ultimate moment per unit length
r_o	radius of column or loaded area
r_p	radius to the loading
r_w	radius of punch
r_y	radius within which all flexural reinforcement yield
r_3	radius of a slab
s	side dimension of slab specimen
v_u	nominal shear capacity
x	neutral axis depth
z	lever arm
α	angle of inclination of the concrete force at the column face
ϵ_c	concrete strain
ϵ_{c1}	$0.85\ f'_c/4700\sqrt{f'_c}$
ϵ_{ct}	concrete tangential strain
ϵ_{cu}	concrete ultimate strain
ϵ_{st}	steel tangential strain
ϵ_{sy}	yield strain of reinforcing steel

ρ	reinforcement ratio (A_s/bd)
ρ_r	ratio of radial reinforcement
ρ_t	ratio of tangential reinforcement
Φ_o	P_u/P_{flex}
$\Delta\Phi$	small sectorial angle of a radial segment
ψ	rotation of the slab portion outside the shear crack
ψ_f	rotation at failure

Chapter 1

Introduction

In recent years, considerable attention has been given to the use of silica fume as a partial replacement for cement to produce high-strength concrete. High-strength concrete is used for offshore platforms, marine structures, bridges, tall buildings and long span bridges. Recently, a gravity based structure utilizing high-strength concrete has been recommended for the Hibernia development off the eastern coast of Newfoundland. High-strength concrete, containing mineral admixtures such as silica fume, is relatively impermeable. Hence, it offers great promise for the durability problem associated with marine and offshore structures situated in the harsh North Atlantic waters. Furthermore, the compressive strength is the fundamental basis for design and quality assessment, and has a major impact on the cost effectiveness of each platform.

In spite of the wide use of high-strength concrete, very little information is available on the material and structural behaviour of this material. In the last decade, some research has been conducted on the structural behaviour of high-strength beams. However, to the best of the author's knowledge, no investigation has been reported on the two way slab structural behaviour and punching characteristics of

1

high-strength concrete.

The present building code specifications for shear strength of reinforced concrete slabs are based on the test results of slabs made with relatively low compressive strengths, varying mostly from 14 to 40 MPa. These design provisions may not apply to situations involving parameters different than those upon which the empirical equations are based. Hence, it is necessary to re-examine the present shear design methods as they apply to high-strength concrete.

Offshore concrete platforms have proven their worth in the harsh North Sea environment for the past decade. They now face the additional challenges posed by the North Atlantic and the Arctic Offshore frontiers. Offshore structures frequently have a concrete perimeter wall which is normally designed to resist the impact of ice on the structure. Both flat and curved exterior walls have been used. Thus, the concrete plate and shell panels represent the most predominant structural element ed in the walls of concrete offshore platforms.

The present research, triggered by the potential development of offshore oil exploration for Hibernia, includes a part of a research programme at Memorial university, in which the use of high-strength concrete, as a structural material for potential arctic and sub-arctic structures, is being investigated.

1.1 Scope

The main objective of the material investigation is to determine the basic mechanical properties of high-strength concrete containing silica fume and fly ash. A high-strength concrete mix was developed using local aggregates and conventional cement. The mix had to be suitable for offshore applications. The effect of cold

ocean water on the mechanical properties of high-strength concrete containing silica fume and fly ash was also studied.

The present research investigation addresses the structural behaviour of two way-slab systems made with high-strength concrete. Fifteen high-strength concrete slabs and two normal strength concrete slabs, were tested. The slabs were symmetrical and they were loaded through a column stub by a hydraulic actuator in displacement control. Different measurements (deformations, strains, etc.) were collected during the course of testing. The behaviour of the slabs were observed and the test results and observation were analyzed.

Based on the strain measurements and test results, a mechanical model was developed to predict the ultimate capacity of high-strength two-way slabs. The model uses the strain compatibility and equilibrium equations of an assumed failure criteria.

1.2   Objectives

The main objectives of this research investigation can be summarized as follows:

1. To develop a high-strength concrete mix, for offshore applications, using conventional cement and aggregates available in Newfoundland.

2. To study the mechanical properties of high-strength concrete containing silica fume and fly ash.

3. To investigate the effect of cold ocean water, simulated under laboratory conditions, on the mechanical properties of green high-strength concrete containing silica fume and fly ash.

4. To examine the structural behaviour of two-way slabs.

5. To determine the deformation characteristics (deflections, rotations, and strains) of two way slabs.

6. To correlate between flexural strength and punching stress resistance of two-way slabs.

7. To study the effect of the different parameters (concrete strength, flexural reinforcement, loading area/span ratio, etc.) on the punching shear capacity of two way slabs.

8. To develop a rational mechanical model for the prediction of punching shear of high-strength simply supported two-way slabs.

1.3   Thesis Outline

Chapter 2 is divided into two parts. The first part reviews the use of concrete structures in an ocean environment and addresses recommendations for a durable mix. The second part reviews previous research conducted on two-way slabs including both empirical and rational approaches.

Chapter 3 contains the material investigation phase of the research. It deals with the development of high-strength concrete mix, suitable for offshore applications. It also presents the mechanical properties of the high-strength concrete containing fly ash and silica fume, and the effect of low temperatures on these mechanical properties.

Chapter 4 describes the two-way slab experimental investigation. Details of experimental facilities, test procedures and instrumentation are presented.

Chapter 5 presents the test results and observations obtained from the experimental investigation, the analysis of these results, and comparison of ultimate loads obtained from the tested slabs with different codes predictions.

Chapter 6 deals with the theoretical formulation and development of the adopted mechanical model.

Finally, a summary of the investigation and the conclusions reached are given in Chapter 7.

Chapter 2

Review of Literature

2.1 Concrete for Marine and Offshore Structures

Concrete has been successfully used in marine environment for centuries. It has been employed in the construction of piers, bridge foundations, retaining walls and breakwaters. In 1971, concrete was first introduced on a large scale to oil industry with the construction of Ekofisk 1, the first concrete Gravity Based Structure (GBS) installed in the North Sea. It was constructed in 70 m deep water and contained 80000 m^3 of nominal strength concrete with a specified 28-day compressive strength of 45 MPa. Since that time, over twenty other concrete gravity platforms have been constructed in the North Sea, the Baltic Sea and offshore Brazil [1].

The main desirable characteristics of the concrete used for platform construction are [2]: (a) strength, (b) durability, and (c) constructibilty. Based on these criteria, high-strength concrete offers great promise for offshore structures. High-strength concretes (50 to 70 MPa), containing water reducing and mineral admixtures, are relatively impermeable and offer an excellent solution to the problem of durability of concrete in a seawater environment. Furthermore, the compressive strength is the fundamental basis for design and quality assessment, and has a major impact

on the cost-effectiveness of a platform.

2.1.1   Durability of Concrete in Marine Environment

Several research workers [3, 4, 5, 6] studied the case histories of deteriorated port-land cement concretes exposed to sea water, in both mild and cold climates, for different exposure ages up to 67 years. It was concluded that the permeability of concrete was the most important characteristic determining its durability. Mehta [4] showed that, depending on the tidal lines, the individual process of deterioration tend to limit itself to different parts of a structure. From this standpoint, a marine structure can be divided into three zones as illustrated in Fig 2.1. The upper most part (atmospheric zone), which is above the high-tide line, is not directly exposed to sea water. However, it is exposed to atmospheric air, winds carrying salts and frost action. Consequently, cracking due to corrosion of the reinforcement and/or freezing and thawing of concrete are the predominant phenomena causing deterioration in this zone. The concrete in the splash zone, which is between the high and low-tide marks, is not only vulnerable to cracking and spalling of concrete due to wetting and drying, frost action, and corrosion of reinforcement, but also to loss of material due to chemical decomposition of hydration products of cement, and impact of waves containing ice, sand, and gravel. The lower part of the structure (submerged zone), which is always submerged in sea water, is vulnerable to strength retrogression and loss of material as a result of the chemical reaction between sea water and hydration products of cement.

Generally speaking, for long-time durability of coastal and offshore structures, the concrete must show resistance to; thermal cracking, frost action, abrasion/erosion
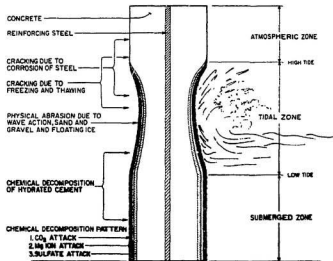
Figure 2.1: Deterioration of a concrete structure in sea water [Mehta 1980]

loss and expansive chemical and electrochemical phenomena (such as alkali-aggregate reaction and corrosion of reinforcing steel). The permeability of concrete is the most important factor in all the three zones because it influences all physical and chemical phenomena causing concrete deterioration.

2.1.2 Selection of Materials

In the United States and Canada, the ACI Committee 357 (ACI 357 R-84) [7] report is used for the design and construction of fixed and prestressed concrete structures for service in a marine environment. In Europe and Asia, for the design and construction of concrete in sea structures it is customary to use the recommendations of the International Federation of Prestressed Concrete Structures (FIP, 4th edition 1984) [8]. Although both the ACI and FIP recommendations were published quite recently (1985), it is not surprising that the recommended practice lags behind the current (1986-1989) field practice at the North Sea. A sufficient amount of published data is now available from field experience in the North Sea where twenty offshore concrete platforms have been constructed during the period 1972-1987 [9, 10].

2.1.2.1 Cement

The ACI 357 R-84 maximum limit of 10 % C_3A content is based on the assumption that cements with higher than 10 % C_3A are susceptible to sulphate attack. Some researchers have questioned the validity of such an assumption; Mehta [4] cited three case studies where no sulphate attack was observed in long time (46 to 67 years) sea water exposure of concrete containing 14 to 17 % C_3A and he attributed

that to the low-permeability of these rich mixes. Mather [5] confirmed that concrete prisms made with a high C_3A (12.5 %) ASTM Type III portland cement did not show any lack of chemical durability after more than 30 years of exposure at Treat Island, Maine. As for the current field of practice at the North Sea, the heat of hydration and permeability consideration require that, respectively, the use of ASTM Type III and Type V portland cements may be discouraged and the use of portland-pozzolana cements and portland-blast furnace slag cements are to be given special consideration. In general, Mehta [11] recommended that the use of any portland cement having 6 - 12 % C_3A content for concrete sea structures should be satisfactory provided that the cement is compatible with the admixtures to be used.

Both the FIP and ACI recommendations require a minimum cement content of 360 kg/m³; however the former recommends a minimum of 400 kg/m³ cement for the splash zone concrete mixture. The use of high cement content in massive structures frequently leads to thermal cracking, which has the effect of increasing the permeability and reducing the durability. In order to avoid this problem, the Norwegian Offshore concrete practice has developed a high-strength cement with moderate heat of hydration. In general, adequate measures should be taken to control the temperature gradients in concrete in order to prevent thermal cracking.

The maximum allowable water cement (w/c) ratio recommended by ACI for marine structures is 0.45 for the submerged zone, and 0.40 for the splash zone and the atmospheric zone. FIP requires a maximum w/c cement ratio of 0.45 but prefers the use of 0.40. In the North Sea field practice, a w/c ratio of 0.45 was used in the Beryl A concrete platform and was reduced to 0.38 in Gullfaks C concrete

platform.

2.1.2.2 Admixtures

The FIP recommendation provides that high-quality pozzolanic materials, such as silica fume may be added to produce improved strength, durability and workability. However, contrary to the sufficient evidence from both laboratory and field practice, the ACI 357 R-84 does not appear to take a clearly supportive stand in favour of the use of pozzolanic and cementitious admixtures in concrete sea structures. Some recent publications and research undertaken by Canada Centre for Mineral and Energy Technology (CANMET) provide a wealth of useful information on the composition and properties of these concrete admixtures [12]. These publications reveal the advantages of using pozzolanic admixtures; these pozzolanic admixtures help in improving the workability, reducing the heat of hydration, and increasing the strength of the transition zone between aggregate and cement paste. The fine particles of a mineral additive are also able to enhance the homogeneity in the hardened concrete microstructure, thus improving the ability of concrete to resist microcracking, which is important for maintaining the impermeability during service. The amount of a mineral additive needed for this purpose varies with its particle size and chemical composition. Several studies [13, 14] recommended a fly ash replacement of 12 to 25 % by weight of total cementitious materials. Whereas, 5 to 10 % condensed silica fume is adequate due to its exceedingly small particle size. Similarly, to enhance the homogeneity in the hardened concrete microstructure, it is essential to use a low water-cement ratio and to obtain a proper dispersion of the cementitious materials in a fresh concrete mixture. Water-reducing admixtures are

commonly used for this purpose. In earlier work (Beryl A, 1974), a lignosulfate-type water reducing agent was employed . It contained certain impurities which caused considerable air entrainment and excessive retardation in fresh concrete. High-purity naphthalene or melamine sulphonate type water reducing admixtures should be used in concrete mixtures when resistance to internal cracking due to freezing and thawing cycles is desired. Pig n et al. [15] reported from laboratory tests on concrete containing 9 % condensed silica fume and 0.3 water/cement ratio (w/c), that enough freezable water is present in these low w/c ratio concrete to cause damage in freezing and thawing tests, unless air entrainment was used.

The desired air content recommended for marine structures is normally in the range of 4 - 6 %. Recently, the air entrainment is specified as an air-void system instead of the total air volume. A minimum spacing factor 0.25 mm, a specific surface area of 25 mm^2/mm^3 and an air void-content of at least 3 % are generally recommended by the Norwegian Offshore concrete practice [10].

Both ACI and FIP warn that when two or more admixtures are used, their compatibility with the cement and aggregate types should be examined. Also to protect reinforcing and prestressing steel from corrosion, no $Ca\,Cl_2$ or admixtures containing chlorides should L used.

2.1.2.3 Aggregates

ACI permits the use of any natural sand and gravel or crushed rock that conform to ASTM C33 specifications for concrete aggregates. FIP recommends that aggregates likely to undergo physical or chemical changes should be avoided. The North Sea field practice is the only specifications which requires the use of high-quality

aggregates. The maximum size of aggregate used in the construction of concrete structures in the North Sea is limited to 20 mm, while the recommended practice in both ACI and FIP makes no attempt to suggest a relationship between the maximum size of aggregate and the permeability of concrete. The aggregate grading used in the North Sea is achieved by a strictly controlled process. Two different sizes are used to classify the aggregates; 0-5 mm for the fine aggregates and 5-20 mm for the coarse aggregates. Both ACI and FIP do not require any special grading for the concrete used in marine environment.

The incorporation of a highly reactive pozzolanic material, such as condensed silica fume improves considerably the aggregate-cement paste bond and consequently, the abrasion/erosion resistance of the concrete [16].

2.1.2.4 Compressive Strength

Concrete quality is generally described by its compressive strength. In the design process this property is also the key parameter although other strength properties must be considered. The minimum specified strength required by ACI is 35 MPa for all zones and 42 MPa where severe surface degradation is likely. The modern concrete offshore structures in the North Sea are built with high-strength concrete, the minimum, being a 60 MPa concrete [10]. For instance, the specified strength (56 MPa) for Gullfaks C (1986-87) concrete is 50 % higher than the strength of Beryl A (1973-75) concrete (36 MPa). The actual 28-day compressive strength of the Gullfaks concrete core samples was found to be approximately 70 MPa. This indicates that the compressive strength specified by the North American specifications is lagging behind the North Sea field of practice by almost 15 years.

2.2 Punching Shear Strength of Concrete Slabs

2.2.1 Introduction

Research on punching shear has yielded a number of methods by which the ultimate shearing strength of slabs can be predicted. In general, the various suggested approaches can be described as either the results of an empirical study, in which a statistical analysis of the available test results is used to establish a relationship between the load or stress at failure and parameters of the slab, or the result of a rational study, in which the strength of the slab materials and the mechanism of failure are idealized and described mathematically.

2.2.2 Empirical Studies

In an investigation of wall and column footings, Talbot [17] proposed an empirical equation for design against punching expressed in terms of the nominal shear stress at a critical perimeter at a distance d from the column face:

$$v = \frac{V}{4(c + 2d)jd} \tag{2.1}$$

where v is the ultimate shear stress, V is the ultimate shear force, c is the side dimension of a square column, d is the effective depth of the slab and jd is the lever arm of the internal resisting moment of the slab. According to Talbot, punching shear failure is mainly due to diagonal tension and hence the limit for v should be proportional to f_t and consequently proportional to f_c'. This equation contradicts the experimental findings since, as the reinforcement ratio increases, the predicted punching shear decreases.

In 1938 Graf [18] reported the results of his experimental study on slabs sub-

jected to concentrated loads and this was followed by the work of Forsell and Holemberg [19] in 1946. Their formulation was similar to that of Talbot's except for the location of the critical section. According to Graf, the critical section was at the column periphery, while Forsell and Holemberg located the critical section at a distance $h/2$ from the column face. In the latter case, the shear stress distribution over the slab thickness is assumed to be parabolic;

$$v = \frac{V}{4ch} \qquad \text{(Graf)} \qquad (2.2)$$

$$v = \frac{V}{4(c + \frac{h}{2})h} \qquad \text{(Forsell and Holemberg)} \qquad (2.3)$$

Hognestad [20], in 1953, was the first to propose a design equation in which the influence of flexural strength on the ultimate shearing stress was recognised. After a re-evaluation of Richart's [21] tests on column footings, Hognestad showed that the design methods of the time (based on Eq. 2.1) did not give a consistent factor of safety with respect to shearing failures. He suggested that ultimate strength of slabs failing in shear is mainly dependent upon the following variables:

1. Properties of the materials used in the slab:
    (a) quality of concrete as expressed by the cylinder strength f_c';
    (b) amount, type, and quality of tension and compression reinforcement.

2. Size and shape of the loaded area as compared to the slab thickness.

3. Span, support condition and edge restraints of the slabs.

Hognestad found that the ultimate shearing stress of a variety of slabs can be expressed by the empirical equation;

$$v = (0.035 + \frac{0.07}{\Phi_o})f'_c + 130 \quad \text{psi} \tag{2.4}$$

where Φ_o is the ratio of the ultimate shearing capacity of the slab to the ultimate flexural capacity of the slab if it had not failed in shear. The ultimate flexural capacity of the slab was computed using yield line theory and was dependent on the properties of the slab and the size and position of the loaded area. Hognestad conceded that Equation 2.4 might not be valid if used for slabs with dimensional ratios or concrete strengths outside the ranges of those of Richart's slabs.

In 1953 Elstner and Hognestad [22] reported shear tests of a further 24 slabs. Equation 2.4 was reviewed in the light of these tests and those reported by Forsell and Holemberg [19] and Richart and Kluge [23]. Satisfactory agreements between observed and predicted shearing failure loads were found to exist.

After carrying out additional tests in order to extend the ranges of the slab variables of previous test programmes, Elstner and Hognestad [24], in 1956, reported that Eq. 2.4 gave unsafe estimates of the ultimate shear strength of slabs of high-strength concrete. The following equation was found to be in better agreement with the test results.

$$v = \frac{0.046}{\Phi_o}f'_c + 333 \quad \text{psi} \tag{2.5}$$

It was also reported that neither a concentration of tensile reinforcement directly beneath the loaded area nor the presence of compression reinforcement had any appreciable effect on the ultimate shearing strengths of the concrete slabs tested.

Moe [25] conducted an experimental investigation consisting of five different series of test slab and studying the effect of:

1. Casting holes in the slab in the column vicinity.

2. Concentrating the tensile reinforcement over the column.

3. Including special types of shear reinforcement.

4. Extreme column size.

5. Eccentric column loads or transfer of moment.

Moe then, based on his experimental program, developed a semi-empirical type equation to calculate the ultimate shear strength;

$$v_u = \frac{P_u}{cd} = \frac{15(1 - \frac{0.075}{d})\sqrt{f'_c}}{1 + \frac{5.25cd\sqrt{f'_c}}{P_{flex}}} \quad \text{psi} \tag{2.6}$$

In conclusion Moe stated that the critical section of a slab, subjected to a concentrated load, was at the column perimeter and that the shear strength is to some extent dependent upon the flexural strength.

In the report of ACI-ASCE committee 326 [26] of 1962, the recommendations of the existing building code were reviewed in the light of all the research carried out at that time. It was suggested that Moe's equation (Eq. 2.6) was the best equation to date for the prediction of the failure load of slabs tested under laboratory conditions. For practical design, Φ_o was considered to be an unimportant variable and, because it should always be equal to unity, it was eliminated from Moe's equation by assuming that it was equal to unity. Following Moe's suggestion that the shearing strength is a function of the square root of the concrete compressive strength,

the Committee recommended that the following design equation for the calculation of the ultimate shear load:

$$V = vbd \tag{2.7}$$

where $v \leq 4.0\sqrt{f'_c}$ and b is the length of the "pseudo critical section," taken as the perimeter at a distance of $d/2$ from the periphery of the loaded area. The position of the assumed critical section was chosen so that Eq. 2.7 incorporates allowance for the c/d ratio.

2.2.3 Rational Studies

Based on observations of a number of tests of circular slabs with central columns, Kinnunen and Nylander [27] conceived an idealised model of a slab at punching failure. It was assumed that the slab portion outside the shear crack, which is bounded by this crack, by radial cracks, and by the circumference of the slab, can be regarded as a rigid body which is turned under the action of the load around a centre of rotation located at the root of the shear crack. The model is illustrated in Fig 2.2.

The criterion of failure in the mathematical model was the collapse of the conical shell which occurred when the tangential strain on the surface of the slab in the vicinity of the root of the shear crack reached an empirical critical value. The characteristic tangential strain at failure was determined from tests on slabs with ring reinforcement only. The punching load was calculated by assuming a dimension of the conical shell and then following a convergent iterative process.

Kinnunen and Nylander found that their theory gave values for the punching load which were in satisfactory agreement with results of their own tests as
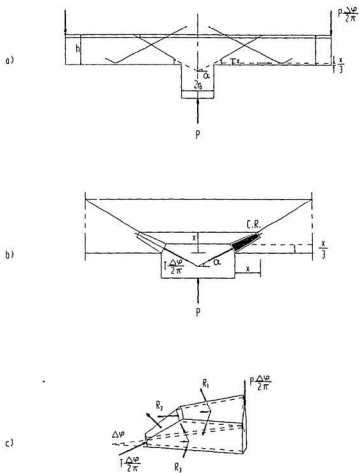
Figure 2.2: Punching model adopted by Kinnunen and Nylander

well as those of Elstner and Hognestad [24]. They attributed low calculated values, in the case of two way reinforcement, to dowel and membrane effects, and suggested that they should be taken into account by multiplying the calculated ultimate load by 1.1.

Kinnunen [28] later published a paper in which he presented a prima ly qualitative study of dowel and membrane action in slabs with two-way reinforcement, and concluded that the punching load is increased by about 20 per cent by dowel and membrane effects.

The theory of Kinnunen and Nylander has been criticized by Long [29] and Reimann [30]. Their major common objection was that the assumption that the compressive strength in the conical shell was approximately constant throughout, was made in neglect of probable shearing stresses on the shell surface. This criticism implies that the existence of the assumed conical shell should have been proven. Rather than verifying its existence, Kinnunen and Nylander have justified its use, along with that of their criterion of failure, by showing consistent satisfactory agreement between calculated and test punching loads.

Based on the test observations of Kinnunen and Nylander [27], Reimann [30] proposed a simple idealised model of slab at punching failure from which the punching load can be calculate directly. The theoretical model is made up of a punched cone of concrete, an outer annular slab and a joint, which was idealised as a hinge bridged by a spring, between the inner and outer regions at the periphery of the column. The hinge was assumed to coincide with the centre of rotation of the annular slab. The model is illustrated in Fig 2.3. Reimann applied his method of analysis to results of tests by Kinnunen and Nylander and others. He found reasonable
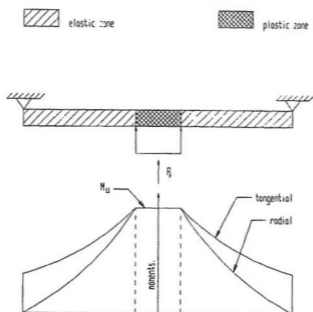
Figure 2.3: The mechanical model proposed by Reimann

agreement between calculated and test failure loads although the average values of the ratio of the actual failure load to his calculated failure loads were usually greater than unity. Reimann ignored any dowel and tensile membrane effects and this could account for his somewhat low calculated values.

In 1967, Long [29] and Long and Bond [31] reported a theoretical method for the calculation of the punching load of a slab with two-way reinforcement. Assuming a linear distribution of stress, the stresses in the shear-compression zone were calculated using thin plate theory. An octahedral shear stress criterion of failure was used to find the stresses at failure and from that an uncorrected load was calculated. The uncorrected load was then adjusted to give the punching load by applying corrections for surrounding slab and support conditions and for dowel and tensile membrane effects.

Long and Bond showed that their theory gave punching loads in good agreement with test results of, among others, Richart [21], Elstner and Hognestad [22], Moe [25] and Kinnunen and Nylander [27].

In the discussion which followed this work, the relevance of the equations of elasticity to slabs near failure and the suggested mechanism of punching failure was questioned. The assumption of Long and Bond that the load supported by a failed slab approximates the effect of dowel and tensile membrane action on the failure load is also questionable.

Masterson and Long [32] later developed this approach and proposed a simplified finite element model for local slab conditions at ultimate failure. Their idealized representation of the slab-column connection was equivalent to the theory of development of local plasticity at the column periphery. By relating the applied load to

the internal moment at failure and by making an appropriate allowance for dowel and membrane effects, the punching strength was found to be well predicted for the majority of chosen realistic slab-column specimens tested by some researchers.

Long [33] later formulated a two-phase design procedure in which the punching strength was predicted as the lesser of either a flexure or shear criterion of failure. This approach has certain limitations, as it could not handle slabs with high-strength concrete and slabs with low level of reinforcement.

In 1987, Long [34] extended his work by using a more rational treatment of the flexural mode of punching failure. Long used an analytically based linear interpolation moment factor to relate the ultimate flexural capacity to the yield moment. This factor depended on the slab ductility which was considered to control the degree of yielding in the slab at failure. The ultimate shear capacity was based on an empirical relationship for vertical shear stress on a critical section close to the column perimeter.

In 1970, Gesund and Dikshit [35] used yield line theory of Johansen (1962) to analyze punching failures in slabs. Their work was based on the research carried out by Gesund and Kaushik [36] who concluded that the ratio P_{flex}/P_{test} for 106 alleged punching shear failure averaged 1.015 with a standard deviation of 0.248. They assumed a yield line fan mechanism around the column, as shown in Fig 2.4. The ultimate load calculated for that mechanism was considered to be the ultimate punching load for the case of an interior circular column. This method overestimates the punching strength unless the flexural mode of failure is the dominant one.

Another application of plastic theory to estimate the punching resistance of axisymmetric concrete slabs without shear reinforcement was presented by Nielsen,
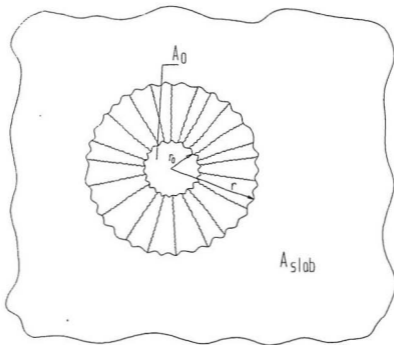
Figure 2.4: Yield line mechanism used by Gesund *et al.* [35,36]

Braestrup et al. [37] in 1978. This theory is in contrast with Gesund's method, as the punching mechanism adopted (Fig 2.5) is totally independent of the flexural properties of the slab. The mechanism is one of the punching out of a solid of revolution attached to the column, while the rest of the slab remains rigid. Using minimization of work together with the modified Coulomb criterion and the normal flow rule (Fig 2.6), the minimum upper bound solution for the ultimate punching load was obtained. This theory contradicts experimental findings as it neglects the effect of the flexural reinforcement on the ultimate punching capacity of the slab.

In 1982 Andrä [38] presented a theoretical model for the punching shear of a circular slab with ring reinforcement. A finite element analysis was used to derive the proposed model. As in Kinnunen and Nylander, this model considers the rigid body rotation of radial segments around a center of rotation located at the face of the column and the neutral axis, as shown in Fig 2.7. Each segment is analyzed using a truss model (Fig 2.7) beyond the shear crack, with 45° tension and compression elements representing the behaviour of the uncracked web. Superimposed on this lattice there are additional compressions radiating from the column face below the crack.

Fig 2.7 shows the failure philosophy assumed by Andrä. He describes the failure of the concrete strut near the column face as being a restricted crushing of concrete, while, in the part of the strut far from the column face, its character is of an unrestricted splitting.

Shehata [39], in 1985, followed by Shehata and Regan [40] in 1989, presented a model which they claimed to be an improvement over that of Kinnunen and Nylander. In that model, the effect of dowel and membrane was directly calculated

Figure 2.5: Failure mechanism of Nielson *et al.* [37]

a) Modified Coulomb failure criterion

b) Yield locus in plane strain

Figure 2.6: Failure criterion and yield line locus for concrete.

a) Rigid body rotation model adopted by Andra.

b) Andra's truss idealization of a radial segment.

c) Failure surface proposed by Andra.
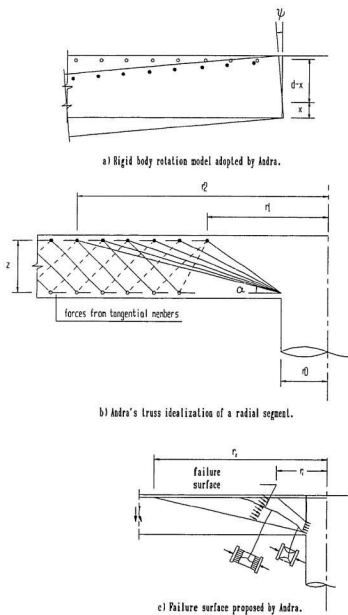
Figure 2.7: Andrä's truss model.

from the model and the failure criterion was modified. This model will be discussed in details in chapter 6 together with its drawbacks.

In 1987, Alexander and Simmonds [41] presented their truss model. The model proposed consisted of a three dimensional space truss composed of concrete compression struts and steel tension ties. The reinforcing steel and concrete compression fields were broken down into individual bar-strut units (Fig 2.8).

The truss model included two types of compression struts: (1) those parallel to the plane of slab (anchoring ties) and, (2) those at some angle α to the plane of the slab (shear struts). The model predicts only two possible failure modes for a shear strut; either the steel yields and the angle of shear strut α reaches some critical value, or the concrete fails in compression prior to yielding of steel. This implies that the traditional concepts of shear and flexure does not apply, and the two possible modes of slab failure should be classified as local connection failures as opposed to overall slab collapse.

In conclusion, Alexander and Simmonds stated that the evaluation of the angle α needed further investigation, as it was based on an empirical equation obtained from the test results.

Interestingly, all of the reviewed rational approaches have been shown to provide satisfactorily accurate estimates of the ultimate punching load, even though in each case fundamental objections to some of the assumptions of the respective authors have been raised.
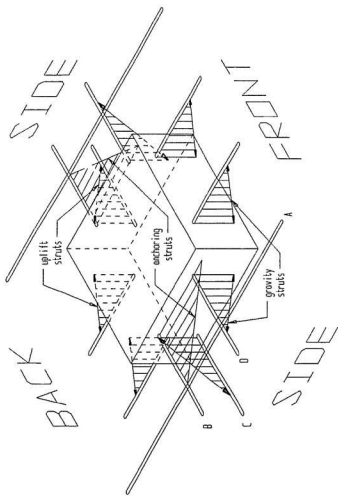
Figure 2.8: The truss model as proposed by Alexander and Simmonds [41]

Chapter 3

Material Investigation

3.1 Introduction

The materials phase of the current research work will be presented in this chapter. The development of the high-strength concrete mix design, for offshore applications, will be described. At the outset, the different materials used in the concrete production are briefly discussed. The trial batches required to identify the optimum mixing proportions and mixing procedure are described. The mechanical properties of the recommended mix were then examined to ensure the suitability for offshore applications. Finally, the effect of low temperatures on the mechanical properties of high-strength concrete is examined.

3.2 Selection of Materials

The production of high-strength concrete that meets the requirement for workability and strength development demands more stringent requirements on material selection than for lower-strength concretes. In this study, local materials are utilized. The selection of these materials was based on the recommendations of earlier researchers and test results from experiments conducted at the concrete laboratory

31

of Memorial University.

3.2.1 Cementitious Materials

The term "cementitious materials" refers to the combined total weight of portland cement and pozzolanic materials (fly ash and silica fume) for the production of high-strength concrete.

3.2.1.1 Cement

Ordinary portland cement (Type 10) CSA3-AS5 with modified C_3A content of about 6 % as produced in Newfoundland was used. As discussed in chapter 2, this C_3A content lies within the acceptable limits of 6–12 % for concrete application in marine environment. Chemical and physical analysis of the portland cement used are given in Tables A1 and Table A2 of Appendix A, respectively.

3.2.1.2 Fly Ash

Class F lignan fly ash from Nova Scotia was used. Chemical and physical analysis of the fly ash are given in Tables A1 and Table A2 of Appendix A, respectively. Class F fly ash is normally produced from burning anthracite or bituminous coal and has pozzolanic properties but little or no cementitious properties. Generally, fly ash improves the workability, retards the time of setting of concrete, lowers the heat of hydration, improves resistance to attack by sulphate soils and may reduce the cost of cementitious materials.

3.2.1.3 Silica Fume

A typical chemical and physical analysis for the silica fume, which was supplied from the only Canadian source in Quebec, are given in Table A1 and Table A2 of Appendix A, respectively. Silica fume is a by-product in the manufacture of ferrosilicon and silicon metal. Because of its extreme fineness and high glass content, silica fume is a very efficient pozzolanic material. Therefore, it is able to react very efficiently with the products of hydration of portland cement to create secondary cementing materials in hydrating concrete. In a silica fume concrete system, the calcium hydroxide produced by the hydrating portland cement is largely consumed in the ensuing pozzolanic reactions. This results in a product with very low permeability and absorption, thus enhancing the resistance to deterioration in aggressive environments.

3.2.2 Aggregates

3.2.2.1 Coarse Aggregate

Local aggregates were used; the coarse aggregate was mostly crushed quartzite sandstone with a minor percentage of siltstone and shale, and with a maximum nominal size of 20 mm. The use of crushed aggregates, rather than round aggregates, is recommended for the production of high strength concrete. Carrasquillo [42] reported that concrete made using round gravel aggregate does not produce as high compressive strength as concretes using crushed aggregates; this was attributed to the reduced aggregate-mortar interface bond strength of natural gravel aggregates.

3.2.2.2 Fine Aggregate

The optimum grading of the fine aggregates for high-strength concrete is determined more by its effect on the water requirements than on physical packing [43]. Blick [44] stated that a sand with a fineness modulus (FM) below 2.5 gave the concrete a sticky consistency, making it difficult to compact. However, sand with an FM of about 3.0 provided the best workability and compressive strength. In the present investigation, the fine aggregate had identical composition as the coarse aggregate, mainly quartzite sandstone, with a FM of 3.1.

Sieve analysis of the aggregates was conducted according to ASTM C 135. Tests for determination of specific gravity and absorption percentage were done according to ASTM C 127 and ASTM C 128, respectively. The results of sieve analysis are plotted together with the curves indicating the limits specified in ASTM C 33 for fine and coarse aggregates as shown in Fig 3.1. The grading and the physical properties of both the fine and coarse aggregates are given in Table 3.1 and Table 3.2, respectively.

3.2.3   Chemical Admixtures

All chemical admixtures met the requirement of ASTM C 494. The compatibility of the admixtures with the choice of cement is a very important consideration so that no slump loss or any undesirable effects in the concrete are created.

3.2.3.1 Air Entraining Admixture

The use of air entrainment is mandatory to assure the durability of high-strength concrete when it is subjected to freezing and thawing as has been discussed in

Table 3.1: Grading of aggregates

Coarse aggregate		Fine agregate	
Sieve size	Cumulative percentage passing	Sieve size	Cumulative percentage passing
19.0 mm	98.23	4.75 mm (No. 4)	99.86
12.7 mm	45.87	2.36 mm (No. 8)	80.67
1.18 mm	17.21	1.18 mm (No. 16)	47.85
4.75 mm	1.120	600 μm (No. 30)	29.28
		300 μm (No. 50)	14.66
		150 μm (No.100)	5.18
		80 μm	1.43
		Pan	0

Table 3.2: Physical properties of aggregates

	Coarse aggregate	Fine agregate
Bulk specific gravity, SSD	2.603	2.671
Apparent specific gravity	2.626	2.695
Absorption, percentage	0.56	0.52
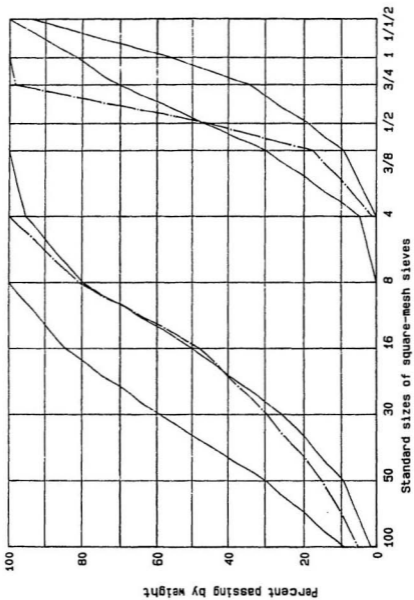
Figure 3.1: Grading of aggregates

chapter 1. In this investigation, a neutralized vinsol resin air-entraining agent conforming to ASTM C 260 was utilized.

3.2.3.2 Retarder

High-strength concrete mix designs incorporate high cement factors which are not common to normal concrete. A retarder is beneficial in controlling early hydration. The addition of water to retemper the mixture will result in marked strength reduction. In the two-way slab testing program, a non chloride water reducing agent of polyhydroxycarboxylic base, conforming to ASTM C 494 Type B and D, was used.

3.2.3.3 High-range Water Reducers

The use of high range water reducing agents, also known as superplasticizers, in high-strength concrete may serve the purpose of increasing strength at slump or increasing slump. Throughout the whole experimental program, a superplasticizer of sulphonated naphthalene formaldehyde base, conforming to ASTM C 494 Type F, was employed.

3.3 Mix Design

The main objectives of the trial mixtures were

- To achieve a 70 MPa class concrete, using locally available materials in the province of Newfoundland.

- To find the best mixing proportions together with best mixing procedure in order to achieve a better properties of fresh concrete, and a higher compressive

strength of hardened concrete.

Previous designs of this high-strength concrete mix conducted by CANMET [13, 14] were used as a preliminary guide. In those studies, the optimum silica fume content was found to be in the range of 5 % to 10 % on the basis of weight, and a 12.5 % replacement of cement by fly ash was recommended. A total of 12 batches were conducted in the present investigation. For most of the mixtures portland cement together with fly ash and silica fume were kept constant at 550 kg/m³, as was the water-to-cement ratio at 0.27. The loss of workability due to the use of silica fume was compensated for by the use of superplasticizer.

The following series of trial mixes were conducted:

- Using a melamine based superplasticizer. However, after few trial batches the melamine based superplasticizer did not give a satisfactory results and it was replaced with a naphthalene based superplasticizer.

- Using different replacement ratios of fly ash and silica fume.

- Using different fine to coarse aggregate ratios.

- Using different water cement ratios.

- Using a retarder instead of the water reducing agent.

The concrete mix proportions are given in Table 3.3. Table 3.4 presents the properties of fresh concrete; that is slump, air content and density, and the compressive strength of hardened concrete at 7, 14 and 28 days.

Slump loss was the major problem faced during the trial mixes. Even when a superplasticizer and a water reducing agent were used, the mix lost its workability

Table 3.3: Mix proportions of one cubic meter for the trial batches

no.	cement	fly ash		silica fume		w $\bar{c}$	w $\overline{c+f+s}$	fine agg.	coarse agg.	admixtures			
										air ent. ag.	super-plast.	water red. ag.	retarder
	kg	%	kg	%			kg	kg	ml	ml	ml	ml
1	400	60	12	40	8	0.46	0.36	650	1100	350	8500	345	–
2	440	66	12	44	8	0.36	0.29	650	1100	350	6600	345	–
3	440	66	12	55	10	0.37	0.29	650	1100	350	7500	345	–
4	440	55	10	55	10	0.36	0.29	650	1100	350	7500	345	–
5	440	66	12	44	8	0.34	0.27	650	1100	350	7500	345	–
6	440	66	12	44	8	0.34	0.27	750	1100	350	7500	345	–
7	440	66	12	44	8	0.34	0.27	750	1100	350	7500	345	–
8	440	66	12	44	8	0.34	0.27	650	1100	350	7500	345	–
9	440	66	12	44	8	0.32	0.25	650	1100	350	7500	345	–
10	440	66	12	55	10	0.32	0.25	650	1100	350	7500	345	–
11	400	60	12	40	8	0.33	0.27	650	1100	350	7500	–	750
12	400	60	12	40	8	0.33	0.27	650	1100	350	7500	–	750

Table 3.4: Properties of fresh concrete and compressive strength for the trial batches

Mix	Prop. of fresh concrete			Comp. strength		
No.	slump	air cont.	density	7 days	14 days	28 days
	mm	%	kg/m^3	MPa	MPa	MPa
1	25	3.85	2403	36	41	45
2	13	3.75	2407	51	48	54
3	50	4.00	2405	41	51	60
4	76	4.00	2401	46	51	62
5	25	3.95	2407	50	57	68
6	76	3.80	2408	40	42	46
7	76	3.80	2408	–	–	51
8	90	3.85	2407	44	54	71
9	13	3.70	2407	40	48	67
10	14	3.70	2407	38	45	68
11	*	3.3	2405	51	55	68
12	*	3.3	2411	47	58	70

* Flowing concrete

after 15 - 20 minutes. In the two-way slab testing program, a retarder had to be employed since more than one batch was required and the concrete had to be flowing for the casting requirements. It should be noted that different mixing procedures were employed in order to find out the optimum mix design. The mixing procedure recommended by CANMET [13] did not give a satisfactory results, when local materials were used, and the mix was very harsh. A new mixing procedure was recommended and it is described in the following sections.

3.4 Adopted Mix

3.4.1 Mix Design Proportions

Based on the trial mixes, an air entrained high strength-concrete can be produced using conventional cement and aggregates from Newfoundland. The incorporation of silica fume and high-range water reducers makes it possible to achieve high strengths at early ages. Compressive strength of 70 MPa at 28 days was achieved for the concrete containing 12 % class F fly ash, 8 % condensed silica fume and a high-range water reducing agent of naphthalene formaldehyde base.

3.4.2 Mixing Procedure

The following mixing procedure was developed for the production of a workable high-strength mix using local Newfoundland materials:

- Charge 100 % of coarse aggregate;

- Batch 100 % of cement;

- Batch 100 % of fly ash;

- Batch 100 % of sand;

- Mix for 3-5 minutes after adding 50 % of estimated water with water reducing agent;

- Prepare a slurry of silica fume, together with 25 % of gross superplasticizer dose and 20 % of water;

- Mix for 5 minutes;

- Add 30 % of mix water together with air entraining admixture;

- Retemper with the rest of superplasticizer dose to target slump.

3.4.3   Properties of Fresh Concrete

Fresh unit weight of the concrete mix was almost constant with an average value of 2400 kg/m^3. The air content in the majority of the mixtures lie within a 0.5 % tolerance of the target 4.0 % value. Slump values were generally at or below the 100 mm target for those mixes incorporating a superplasticizer and low-range water reducing agent, while for those mixtures including a superplasticizer and a retarder, flowing concrete was attained.

3.4.4   Properties of Hardened Concrete

Properties of concrete such as stress-strain relationship, modulus of elasticity and tensile strength are frequently expressed in terms of uniaxial compressive strength of 150x300 mm cylinders. In the past, the expressions available in literature were based on experimental data less than 41 MPa. Recently, new expressions have been proposed for high-strength concrete. One of the objectives of this research

is to select one of the available expressions for high-strength concrete and check it against the experimental values. This expression is to be adopted for the material modelling throughout the study.

Three batches were cast, each batch had eighteen 150 x 300 cylinders and nine 75 x 75 x 300 prisms. Test specimens were cast in three layers and compacted by means of a standard rod. After casting, the moulded specimens were covered with water saturated burlap and left in the casting room at 20° for 24 hrs. They were then demoulded and transferred to the water tank until required for testing.

3.4.4.1 Compressive Strength and Modulus of Elasticity

The compressive strength and modulus of elasticity were obtained from testing 150 × 300 mm cylinders using a 2670 kN (600 kips) Soiltest compression testing machine. The test cylinders were capped with a high-strength sulphur compound on both ends and tested in accordance with ASTM C 39 for compressive strength and C 496 for modulus of elasticity at 7, 28 and 91 days. The strains were measured using an LVDT mounted on the piston of the testing machine and by means of a compressometer. The load deformation curves were plotted automatically by means of a HP plotter.

Failure of the test specimens occurred suddenly in an inclined, nearly flat plane passing through the aggregate and the mortar without bias as shown in Fig 3.2. The failure mode of high-strength concrete in compression was typical of that of a homogeneous material.

The modulus of elasticity was calculated at a stress level which corresponds to about 0.45 f_c'. The descending part of the curve was not recorded accurately

Figure 3.2: Failure surface of a high-strength concrete cylinder

because of the specimen-testing system interaction, since there is no closed-loop testing machine for axial compression testing at M.U.N. However, the descending part of the curve was monitored for some of the test specimens. The maximum recorded strain was found to be 0.0036 for the 150 × 300 mm cylinders. The stress strain curve was steeper and more linear to a higher applied stress to strength ratio than for lower strength concrete.

The strength properties of the adopted mix are given in Table 3.5. A comparison of the experimentally determined values of the modulus of elasticity with those predicted by the expressions recommended by ACI Committee 363 (Eq. 3.1) is given in Fig 3.3.

$$E_c = 3320\sqrt{f'_c} + 6900 \qquad \text{MPa} \tag{3.1}$$

where:

$$E_c \quad = \quad \text{Modulus of elasticity of concrete}$$
$$f'_c \quad = \quad \text{Compressive strength of concrete}$$

3.4.4.2 Tensile Strength

The tensile strength of concrete can be experimentally determined in three different methods. These three methods are: (1) uniaxial tensile test, (2) split cylinder test, and (3) beam test in flexure. The first method of obtaining the tensile strength may be referred to as "direct", and the second and third methods may be referred to as indirect. In the direct test for tensile strength, the specimen is gripped at its ends and pulled apart in tension. In the splitting tension test, a cylinder is loaded in compression on two diametrically opposite sides, and the specimen fails in tension on the plan between the loaded sides. In the beam flexure test (modulus

of rupture test), a rectangular beam is loaded at the centre or third points and the beam fails in bending; the computed tensile stress at failure load is called the modulus of rupture.

In the present study, the flexure strength was obtained experimentally, carrying out tests on two different sets of specimens. The first set, used to obtain the modulus of rupture, was conducted on 30 x 30 x 355 mm beams loaded at midpoint on a 300 mm span. The tests were carried out using a closed loop MTS testing machine. The tests were conforming to the procedure outlined in ASTM. The second set, used to obtain the tensile splitting strength, was conducted on 150 × 300 mm cylinders loaded through a 2670 kN (600 kips) Soiltest compression testing machine according to ASTM procedure.

A comparison of the experimentally determined values of the splitting tensile strength and modulus of rupture, with those predicted by the expressions recommended by ACI Committee 363 (Eqs. 3.2 and 3.3) are given in Fig 3.4 and Fig 3.5, respectively. The experimentally obtained results were found to be in good agreement with the empirical expression adopted by ACI Committee 363 for determining the modulus of rupture and tensile splitting strength.

$$f'_{sp} = 0.59 \sqrt{f'_c} \quad \text{MPa} \tag{3.2}$$

$$f'_r = 0.94 \sqrt{f'_c} \quad \text{MPa} \tag{3.3}$$

where:

f'_{sp} = Tensile splitting strength of concrete

f'_r = Modulus of rupture

Table 3.5: Strength properties of the adopted mix

Batch Code	Compressive Strength MPa			Modulus of Elasticity GPa			Splitting Tensile Strength MPa			Modulus of Rupture MPa		
	7-d	28-d	91-d	7-d	28-d	91-d	7-d	28-d	91-d	7-d	28-d	91-d
B1	55.2	69.5	73.5	28.81	30.78	31.46	3.41	5.36	5.71	5.32	7.71	7.34
	51.8	68.4	71.2	26.26	28.96	29.52	4.15	4.89	5.01	5.42	6.98	6.89
	50.0	65.5	73.8	29.69	33.92	35.29	4.28	4.75	5.18	6.98	6.06	8.26
B2	56.9	69.8	76.7	27.52	29.96	33.13	4.38	4.75	5.98	7.53	7.27	8.55
	57.6	71.4	78.2	29.15	32.82	33.36	3.93	5.22	6.07	7.34	7.05	8.46
	57.4	70.2	79.1	35.38	36.67	38.07	4.21	4.89	5.41	6.79		8.20
B3	56.4	68.5	71.2	29.79	32.62	34.60	4.02	4.75	4.81	5.69	8.63	
	54.3	69.8	72.4	31.59	35.79	36.39	4.22	4.93	4.97	5.32	8.45	7.57
	55.4	64.0	70.5	38.5	40.07	40.24	3.95	4.66	5.18	4.96		8.58
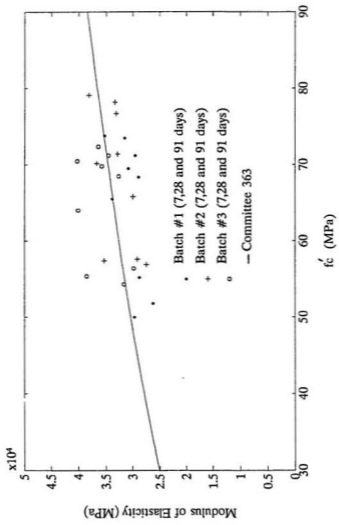
Figure 3.3: Modulus of elasticity versus Compressive strength

49
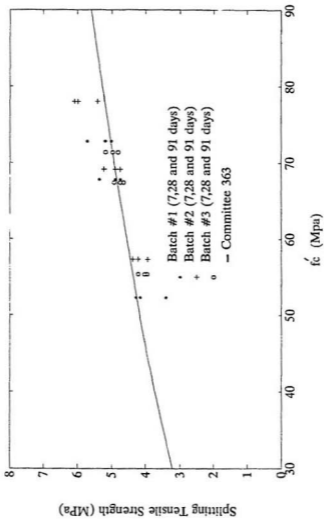
Figure 3.4: Splitting tensile strength versus compressive strength
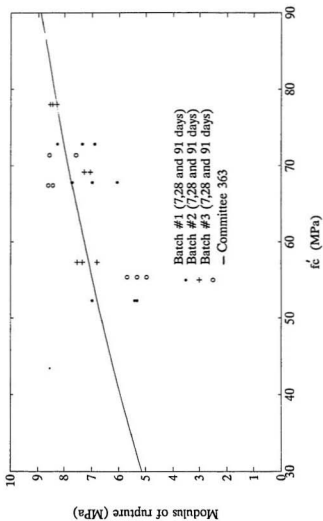
Figure 3.5: Modulus of rupture versus compressive strength

3.5 Effect of Low Temperature on the Properties of High-Strength Concrete

In this section, the effect of cold ocean water on the strength, elasticity and stress-strain relationship of high-strength concrete containing silica fume and fly ash was examined.

3.5.1 Test Specimens

Due to the limitation of the cold storage tanks, the tests were conducted on 75 × 150 mm concrete cylinders. Ordinary portland cement (Type 10) CSA3-AS5 with modified C_3A content of about 6 % as produced in Newfoundland, was used. A 12 % replacement of cement by Type F fly ash and 8 % replacement by silica fume were used on basis of weight, as discussed in section 3.4.

After casting, the moulded specimens were covered with water-saturated burlap and left in the casting room at $20°C$ for 24 hours. Then they were stripped and transferred to five ocean water tanks at 20, 10, 0, -5 and $-10°C$, as shown in Fig 3.6

3.5.2 Compressive Strength

The ratios of compressive strength at various temperatures to that at $20°C$ and 3 days are presented in Table 3.6. At $20°C$, the gain in strength at 91 days was found to be 54 % higher than that at 3 days. At $-10°C$, the strength at 91 days was found to be 8 % less than that at 56. In general, the strength at lower temperatures was found to be less than that at $20°C$ for all corresponding ages. Fig 3.7 represents the same observation in graphical form. To investigate the influence of exposure

Figure 3.6: Water tanks and cooling system used in the study

TABLE 3.6: Ratio of compressive strength at various temperatures
and exposures to the one at 20°C after 3 days

Exposure time in days	Compressive strength (MPa) at 20°C	Ratio of compressive strength at indicated temperature to that at 20°C and 3 days				
		20°C	10°C	0°C	−5°C	−10°C
3	47.90	1.00	0.93	0.89	0.81	0.80
7	58.43	1.22	1.08	1.01	0.99	0.89
14	65.14	1.36	1.24	1.03	0.97	0.95
28	67.06	1.40	1.27	1.07	1.09	0.97
56	69.93	1.46	1.30	1.10	1.06	0.99
91	73.76	1.54	1.34	1.13	1.04	0.91

TABLE 3.7: Ratio of modulus of elasticity at various temperatures
and exposures to the one at 20°C after 3 days

Exposure time in days	Modulus of elasticity E_c (MPa)×10³ at20°C	Ratio of E_c at indicated temperatures to that at 20°C and 3 days				
		20°C	10°C	0°C	−5°C	−10°C
3	29.00	1.00	0.98	0.95	0.93	0.90
7	30.03	1.04	1.02	0.99	0.96	0.93
14	32.51	1.12	1.03	1.00	0.98	0.95
28	34.95	1.20	1.13	1.05	1.03	0.98
56	35.01	1.21	1.13	1.06	1.04	1.02
91	35.80	1.24	1.14	1.06	1.03	1.00
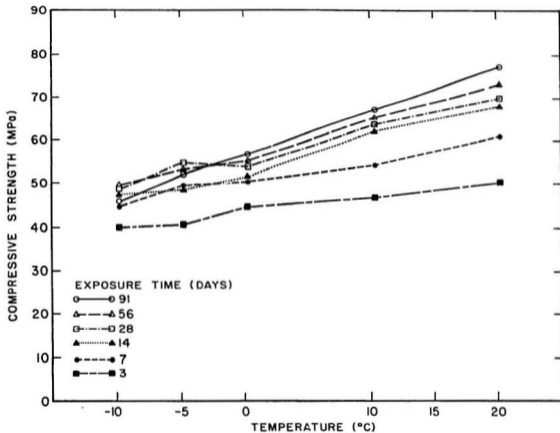
Figure 3.7: Compressive strength versus temperature after exposure of 3, 7, 14, 28, 56 and 91 days

time on the strength under various temperatures, the observed data were analyzed using the least square technique. A logarithmic function in the form of

$$S = a + b \, \log t \qquad (3.4)$$

where, S =   Compressive strength in MPa

t =   Time in days

a, b =   constants

was found to give good agreement with the fitted experimental results. Typical plots of the recorded data versus the fitted functions, regression constants, and coefficients of correlation at temperatures of 20 and $10°C$ are shown in Fig 3.8. Fig 3.9 shows the fitted semi-log relations between compressive strength and exposure time at temperatures of 20, 10, 0, −5, and −10°C.

3.5.3   Elasticity

The modulus of elasticity was calculated at a stress level which corresponds to about 0.45 f'_c. Table 3.7 presents the ratios of modulus of elasticity E_c at different temperatures, to that at $20°C$ and 3 days of exposure.

The values of E_c increased with exposure time. At $20°C$, the values of E_c at 28 and 91 days were found to be higher by 20 % and 24 %, respectively, of the reference values at 3 days. The value of E_c exposed to −10°C at 91 days was decreased by 2 % of that at 56 days. The variation of the modulus of elasticity of concrete with temperature is shown in Fig 3.10.

The values of the modulus of elasticity gave a good agreement with the proposed formula introduced by Carrasquillo et al. [45] and recommended by ACI Committee 363 [43], High-Strength Concrete, as given in Eq. 3.1.
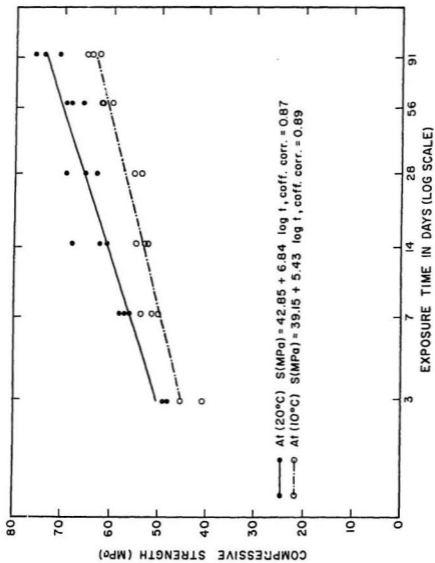
Figure 3.8: Compressive strength versus exposure time at 20 and 10°C
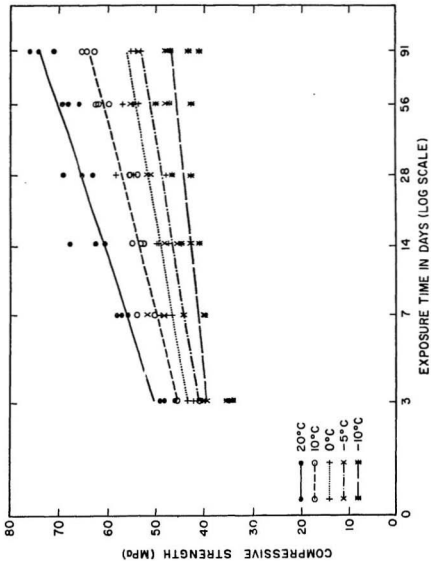
Figure 3.9: Compressive strength versus exposure time at different temperatures
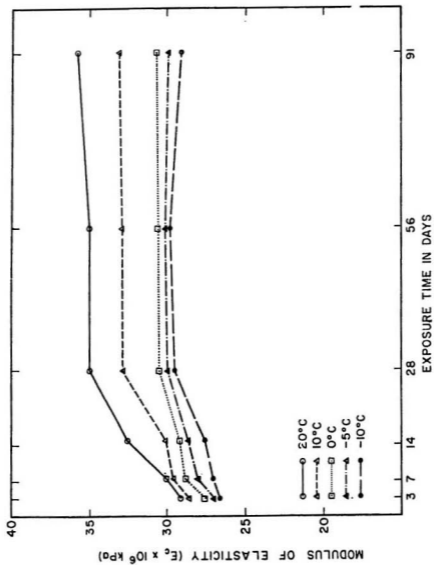
Figure 3.10: Modulus of elasticity versus exposure time

3.5.4   Stress-Strain Relationship

The recorded shape of the stress-strain curve for high-strength silica fume concrete
has a steeper slope and is more linear over a greater range if it is compared with
normal strength concrete. The measured ultimate strain was found to be slightly
higher for the specimens at room temperatures for those exposed to 0, -5, and
$-10^\circ C$. The ultimate recorded strain at room temperature was 0.0036, while for
those exposed to $-10^\circ C$ it was 0.00295 at the same exposure age of 91 days.

Fig 3.11 shows the stress-strain relation at different exposure temperatures.
The characteristic profile of the high-strength concrete stress-strain curves at all
temperatures were found to be in good agreement with an earlier research investi-
gation [45, 46].

3.5.5   Effect of Low Temperatures on the Cement Hy-
drates of High-Strength Concrete

The hydration products of ordinary portland cement concrete at normal tempera-
tures consist mainly of calcium silicate hydrate (C-S-H), hydrates of calcium alu-
minates and calcium aluminate ferrites, and calcium hydroxide. Also, the hydrated
products contain some quantities of unhydrated cement and water in both evap-
orable and non evaporable forms [47].

Calcium hydroxide (hydrated lime), which is a by-product of the hydration
process, reacts at room temperature with the silica fume and fly ash to form to-
bermorite gel, which has a very stable and strong cementing quality. This is called
the secondary hydration process.

The decrease in temperature slowed down the main hydration process. There-
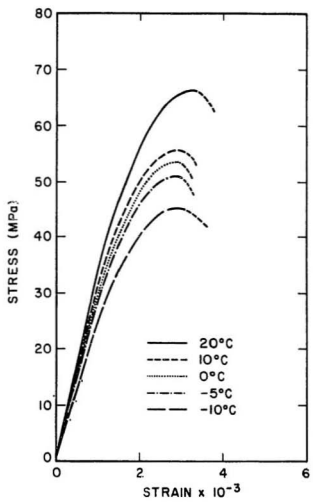
Figure 3.11: Stress-strain curves at different temperatures after 91 days of exposure

fore, the rate of evolution of calcium hydroxide was decreased and, consequently, the secondary hydration process was ceased. This phenomenon can explain the reduction in the rate of maturity due to decrease of temperature, as shown in Fig 3.9. The rate of maturity at $20°C$ is obviously higher than that at other exposure temperatures; the increase in compressive strength at 91 days was about 54 % of that at 3 days. At $10°C$ the gain in compressive strength at 91 days was about 44 % of that at 3 days. For the temperature range of $-5°C$, the rate of maturity was lower than that at room temperature, since the gain in strength was 28 % between 3 and 91 days. The rate was further reduced at $-10°C$ and the gain in strength between 56 and 3 days was only 23.8 %, while there was an 8 % loss of strength between 91 and 56 days.

It is important to note that the test specimens were cured for only one day before exposure to low temperatures. The specimens gained considerable strength after one day of curing due to the richness of the mix used and the low water-cement ratio (w/c). Normally, at this low w/c, the amount of free water is relatively small in the gel pores.

At room temperature, the sulphate attack did not affect the strength of concrete during the duration of the test period. The concrete specimens stored in ocean water and exposed to temperature of $20°C$ and $10°C$ did not show any surface deterioration, as shown in Fig 3.12. The pozzolanic reaction at room temperature helped to remove the free calcium hydroxide and render the alumina-bearing phase inactive. However, the specimens at $-10°C$ showed severe surface deterioration in the structural properties after 28 days, while those at $-5°C$ showed a moderate surface deterioration after 91 days, as shown in Fig 3.13. This surface deterioration

may be attributed to the sulphate attack of concrete for specimens at -5°C and a possible combination of ice damage and sulphate attack for those at -10°C. Since the secondary hydration reaction was ceased at -10°C, calcium hydroxide was free to react with the sulphate. Normally, sulphate reacts with calcium hydroxide and calcium silicate hydrate to form gypsum and calcium sulphoaluminate. These newly formed compounds are structurally much weaker and have greater volume which may lead to the expansion and deterioration of concrete.
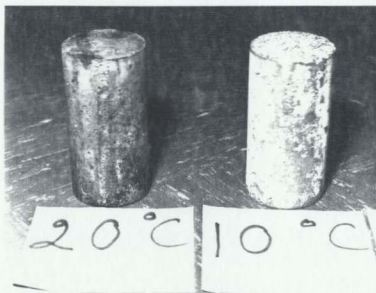
Figiure 3.12: Concrete specimens after 91 days of exposure to ocean water at temperatures of $20°C$ and $10°C$.
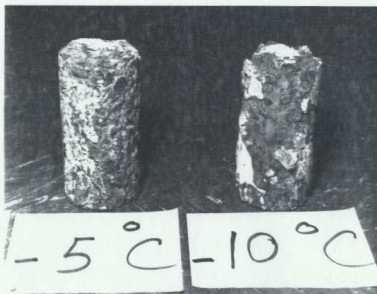
Figure 3.13: Surface deterioration of concrete specimens after 91 days of exposure to ocean water at temperatures of $-5°C$ and $-10°C$.

Chapter 4

Experimental Program

4.1   Introduction

The main objective of this research work, as discussed in the preceding chapters
is to study the structural behaviour and strength characteristics of two-way slabs
made with high-strength concrete and subjected to punching shear.

The test program consisted of testing and evaluation of the structural perfor-
mance of fifteen high-strength concrete slabs and two reference slabs made with
normal strength concrete. Test set up and different equipments used to measure
the deformations and strains throughout the testing program are described in this
chapter.

4.2   Test Slabs

The test specimens were simply supported along all four edges with the corners
free to lift, and were loaded axially through a stub-column. Dimensions and rein-
forcement details of a typical test specimen are shown in Fig 4.1. Full details of
the tested slabs are given in Table 4.1. The slab-column connections tested in this
study are one-to-one full scale model of a typical prototype flat plate structure.
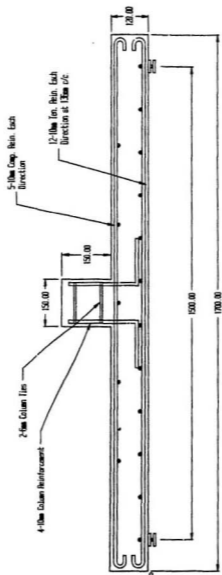
Figure 4.1: Details of a typical test specimen.

All dimensions in mm

Table 4.1 Details of the test slabs

Series No.	Slab No.	Comp. strength MPa	Bar size mm	Bar spacing mm	c mm	Slab thickness mm	Average depth ρ	Steel ratio
	NS1	42	M 10	71.4	150.0	120.0	95.0	1.473
	HS1	67	M 10	214.3	150.0	120.0	95.0	0.491
I	HS2	70	M 10	125.0	150.0	120.0	95.0	0.842
	HS7	74	M 10	88.2	150.0	120.0	95.0	1.193
	HS3	69	M 10	71.4	150.0	120.0	95.0	1.473
	HS4	66	M 15	93.7	150.0	120.0	95.0	2.245
	NS2	30	M 10	125.0	150.0	150.0	95.0	0.944
	HS5	68	M 10	125.0	150.0	150.0	125.0	0.640
II	HS6	70	M 10	125.0	150.0	150.0	95.0	0.944
	HS8	69	M 15	150.0	150.0	150.0	125.0	1.067
	HS9	74	M 15	100.0	150.0	150.0	125.0	1.547
	HS10	80	M 15	71.4	150.0	150.0	125.0	2.240
	HS11	70	M 10	150.0	150.0	90.0	75.0	0.889
III	HS12	75	M 10	93.8	150.0	90.0	75.0	1.422
	HS13	68	M 10	71.4	150.0	90.0	75.0	1.867
IV	HS14	72	M 10	71.4	220.0	120.0	95.0	1.473
	HS15	71	M 10	71.4	300.0	120.0	95.0	1.473

The specimen can also represent the region of negative bending moment around an interior column and the simply supported edges simulate the lines of contraflexure.

Principal variables were slab thickness (Series I, II and III), column stub dimension (Series IV) and concrete strength (slabs NS1 and NS2). The within-series variable was the reinforcement ratio for the slab. For Series I, the six slabs had a thickness of 120 mm and the reinforcement ratio ρ varied from 0.491 % to 2.245 %. Slab NS1 was made with normal strength concrete (42 MPa) and had the same reinforcement ratio, 1.473 %, as slab HS3 (69 MPa). As for Series II, the six slabs had a thickness of 150 mm with a tension reinforcement varying from 0.64 % to 2.24 %. Slab NS2 was made with normal strength concrete (30 MPa) and had the same reinforcement ratio, 0.94 %, as slab HS3 (70 MPa). The three slabs in Series III had a thickness of 90 mm and a reinforcement ratio changing from 0.90 % to 1.86 %. The two slabs tested in Series IV had a column stub of 220 mm and 300 mm respectively. Except for the increased size of column stub and the slight difference in concrete strength, the two slabs were identical to slab IIS3.

4.3   Slab Test Set-up

Fig 4.2 shows a photograph of the test set-up. The loading frame provided external loads applied to the test slabs. The frame was bolted to the floor using a 38 mm base plate and 40 mm anchor bolts spaced at 600 mm apart. The structural floor at M.U.N tructural laboratory is a meter thick reinforced concrete floor. The loading frame consisted of two vertical W-shape columns connected by two horizontal cross channels braced by box shaped construction, and two inclined S-shape columns acting as a brace to the frame.
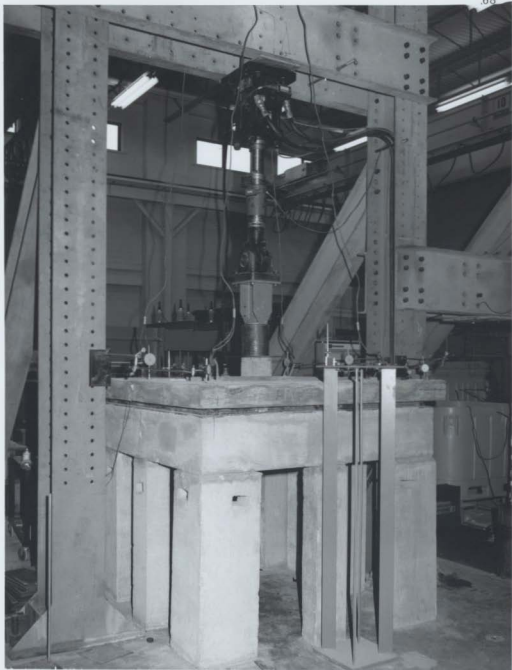
Figure 4.2: Test set up

The supporting reinforced concrete frame, shown in Fig 4.3, was placed on eight reinforced concrete columns so arranged as to give enough space for a person to enter under the slab, observe the cracking pattern, and record different sets of readings.

The slab was supported along the edge on a round steel bar welded to a steel plate fixed to the upper face of the supporting frame in order to simulate a roller support. Rubber packing pieces were provided immediately under the slab surface to insure uniform contact along the supports. A steel protective grid was used under the plates to provide protection for the person observing the cracking pattern.

4.4 Instrumentation and Measurements

4.4.1 Loading System

The load was applied to the test specimen through a hydraulic actuator using an MTS system, as shown in Fig 4.2. The actuator had a piston area of 324 cm² (50.2 in²) with a full stroke of 150 mm (6 in) and a maximum capacity of 670 kN (150 kips).

A closed loop system operating in the displacement control was used for testing the slabs. This system was controlled by means of an MTS controller. The command signal was applied manually by adjusting the set point, while the feedback signal was provided by means of an internal LVDT which was fed to the AC conditioner.
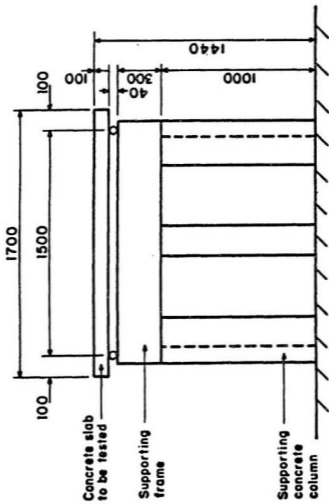
Figure 4.3: Supporting reinforced concrete frame.

All dimensions in mm

4.4.2 Deflections

The deflection of the slabs during loading was measured by a DC linear variable differential transformer (LVDT) which had a linearity of 0.3 % at 10 volts and sensitivity of 16.92 mv/v.mm. Deflections were measured at two locations, namely at the center of the slab and midway from the support line to the center of the slab. The readings were obtained using a multimeter connected to the LVDT. Thereafter, the voltage readings were converted to displacements using the LVDT calibration factor. Furthermore, the load-deflection curves were automatically plotted, using a x-y Hewlett Packard plotter connected to the MTS machine.

The vertical displacements at the plate corners and at the mid-side of the top surface at the support lines were also monitored, using dial gauges with a one-hundredth of a millimetre precision, Fig 4.4.

4.4.3 Steel Strains

The steel strains were measured in each connection at different locations by means of electrical strain gauges. Fig 4.5 shows a typical arrangement of the steel strain gauges. The strain gauges were 10 mm long, with a resistance of 120 Ω, and a gauge factor of 2.04 ± .5 %. For protection against any possible water damage during casting, the strain gauges were coated with a protective sealant and then covered with a shrink tube waxed at the ends.

4.4.4 Concrete Strains

The concrete strains were measured at different locations on the tension and compression faces of the concrete slabs by means of electrical strain gauges. Fig 4.6
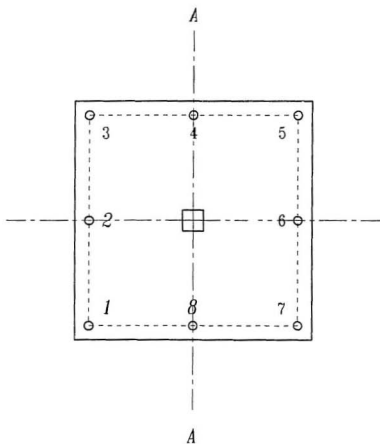
Figure 4.4: Dial gauge locations.
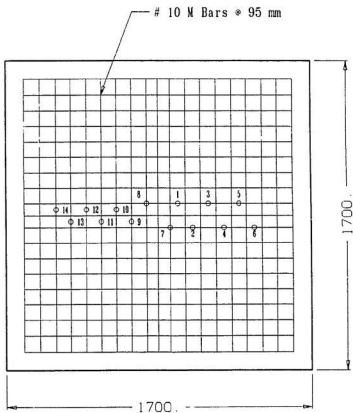
Figure 4.5: Steel strain gauge locations.

All dimensions in mm

shows a typical arrangement of the concrete strain gauges attached to compression face of the slabs. The concrete strain gauges were 50 mm long, with a resistance of 120 Ω and a gauge factor of 2.07 ± .5 %.

A very thin layer of epoxy bonding agent was used to prepare a flat smooth surface on the concrete, to which the strain gauges were glued. The gauges were connected to BLH Electronic (Model 1125) switching and balancing units (wheatstone bridge circuit). The readings, in microstrains, were recorded from four BLH Electronic 1200 Portable Digital indicators; two channel were set for steel gauges and the other two for the concrete gauges. The portable digital indicator is shown in Fig 4.7.

4.5   Preparation of Test Slabs

4.5.1   Fabrication of the Model

4.5.1.1 Concrete

The concrete mix proportions are given in Table 4.2. A 12 % replacement of cement by Type F fly ash and 8 % replacement by silica fume were used on basis of weight for all the test slabs. A superplasticizer of naphthalene formaldehyde bases, a neutralized vinsol air-entraining agent, and a retarder of non chloride base were employed in all the mixes. The target strength was 70 MPa after 28 days. A total of five batches, 0.1 m^3 each, were used in casting each slab.

4.5.1.2 Reinforcing Steel

The reinforcing bars were cold-worked ribbed bars, CSA Grade 400, with a minimum characteristic strength of 400 N/mm^2. The actual characteristic strength was
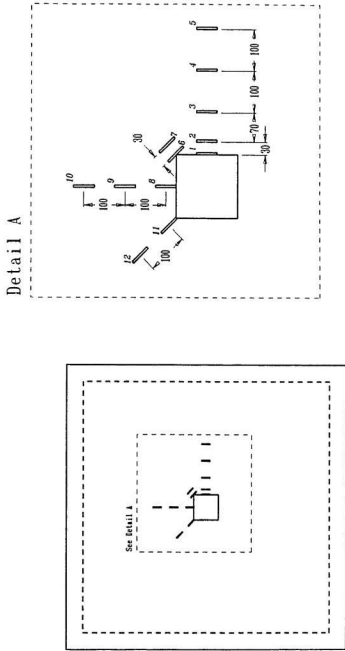
Figure 4.6: Concrete strain gauge location.
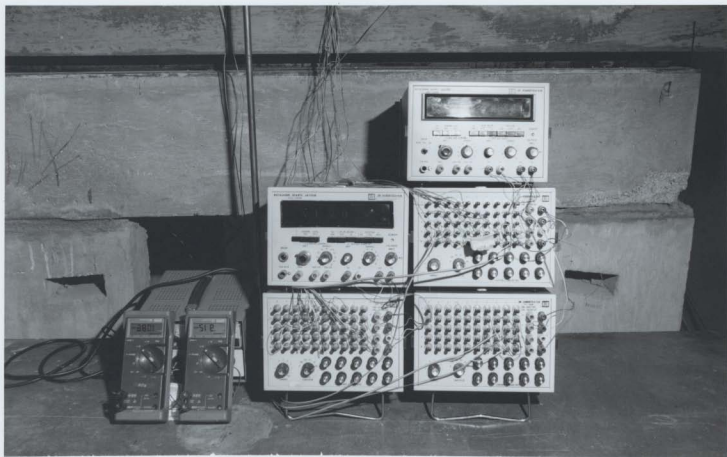
Figure 4.7: Digital strain indicator

Table 4.2: Mix proportions of one cubic meter of concrete used in the two-way slab investigation

Cement	440 kg
Fly ash	66 kg
Silica Fume	44 kg
Cement, Fly ash & silica fume	550 kg
Fine aggregate	656 kg
Coarse aggregate	1100 kg
Air entraining agent	345 ml
Retarder	750 ml
Superplasticizer	7500 ml
w/(c+fa+sf) = 0.27	
Properties of Fresh Concrete	
Slump	flowing concrete
Air content	3.80%
Density	2410 kg/m^3

490 N/mm², with an average ultimate tensile strength of 690 N/mm². A typical stress-strain curve for a reinforcing bar, obtained from a tension test, is shown in Fig 4.8.

4.5.1.3 Formwork

The formwork which was used for casting all the slabs is shown in Fig 4.9. It consisted of a 2000 × 2000 mm deck made with 20 mm plywood, and supported on 50 × 150 mm pine spaced at 400 mm, while the sides of the form were made with 20 mm plywood. The formwork was constructed such that it can be dismantled and re-used. Care was taken in order to keep the slab and the column mutually perpendicular while the model concrete was being poured. The steel was tied together into a sturdy mat and lifted into the form. The reinforcing mat rested upon 20 mm wooden chairs. The chairs were placed far away from the punching zone in order to eliminate their effect on the observed shear strength. However, during concreting great care was taken to insure that the cover provided was uniform.

4.5.2 Casting and Curing

The mixing procedure described in chapter 3 was employed in casting all the test specimens. Each concrete batch was poured into the mould and then vibrated using an electrical rod vibrator. When all the batches were cast, the vibrator was applied to the whole slab to insure its consistency. When full compaction was attained, the top face of the slab was then levelled and finished with a steel trowel. For determining the concrete compressive strength, three 150 × 300 mm (6 × 12 in) cylinders were taken from each batch in conjunction with casting of the principal
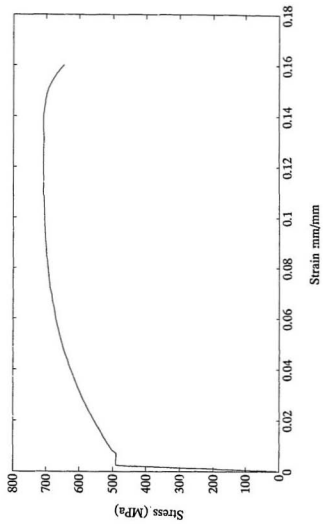
Figure 4.8: Stress-strain curve for a typical reinforcing bar.

Figure 4.9: Formwork used

test specimens.

After casting, the slab and its control specimens were covered with polythene sheeting. The formwork for the slab and the stub column was stripped 48 hours after casting; at the same time the cylinders were demoulded and transferred to a water tank for curing. The slabs were cured for one week by pouring water to its surface every 12 hours.

4.6   Test Procedure

As mentioned before, the tests were carried out using a 670 kN capacity hydraulic actuator provided with displacement control. The load was applied in 8.9 kN (2 kips) increments. During the testing, the slabs were carefully inspected and the cracks were observed at each load increment. Also, the vertical deflection at the center of the slab, corner uplift, concrete strain gauge readings and steel strain gauge readings were recorded at each load increment.

Chapter 5

Test Results and Discussion

5.1 Introduction

The results and observations obtained from testing the seventeen concrete slabs are given in this chapter. In particular, measurements obtained from various systems (as described in chapter 4) are presented in the following sections. In addition, the crack patterns at failure are depicted by means of photographs.

Due to the large amount of experimental data, only a few representative results are used in the presentation of the variation of deflections, strains, etc.

5.2 Load-deflection Characteristics

The applied load versus the deflection at the centre of the slab, for the different test series are shown in Figs. 5.1 and 5.2. The first yielding of the bottom reinforcement is indicated on each curve by a circle, while punching failure is indicated by a downward arrow. The load deflection curves were obtained using the LVDT readings at each load step, while the whole curves were monitored by means of the x-y plotter connected to the MTS machine, as described in section 4.3.1. Table 5.1 shows the measured deflections at the first crack, first yield of tension steel, and

ultimate load for all slabs.

The load deflection curves can be used in classifying the type of failure. Failure modes can be classified into three categories; pure flexural failure, pure punching failure and ductile shear failure. Pure flexural failure takes place in slabs where most of the reinforcement yields before punching occurs and consequently the slab exhibits large deflections prior to failure. Pure shear failure occurs when the slab shows small deflections, with yielding of the tension steel being very localized at the column head. The third type of failure, ductile- shear failure, is a transition between the cases of pure punching and pure flexure failures. The load deflection curves of slabs HS1 and HS11 indicate that they failed by flexure. Nevertheless, none of these slabs reached the state of steadily increasing deflections at constant load, which is characteristic of a normally reinforced concrete specimen experiencing flexure failure. Slabs HS3, HS4, HS9, HS10 and HS13 failed in pure shear as indicated by their load deflection curves.

In general, the load deflection curve for the slabs failing in punching can be represented by two straight lines with different slopes. The first line, has a slope corresponding to the stiffness of the uncracked slab and applies up to the initial cracking load. The second line extends up to the load which caused first yielding in the tension reinforcement. The slope of this line represents the stiffness of the cracked slab (μ).

Within a given series, the stiffness increased as the reinforcement ratio was increased. The effect of the slab depth on the stiffness can be demonstrated by comparing corresponding test slabs in Series II with those of Series I and having the same reinforcement ratio. Series II specimens has stiffness 1.8 times that of
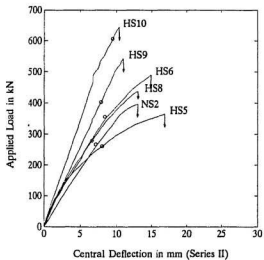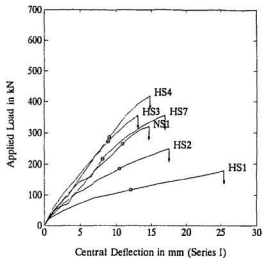
Figure 5.1: Typical load-deflection characteristics at centre span of test slabs (Series I and II)
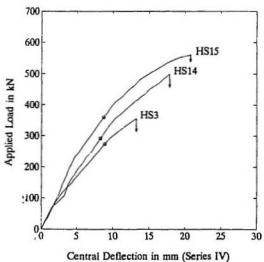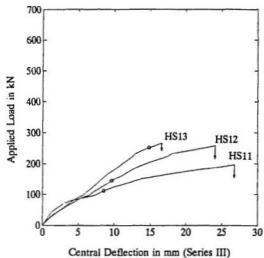
Figure 5.2: Typical load-deflection characteristics at centre span of test slabs (Series III and VI)

Table 5.1: Deflection characteristics of test slabs

Slab No.	Concrete strength f'_c MPa	Steel ratio ρ %	First crack load kN	First crack deflection mm	Yield load P_y kN	Yield load deflection Δ_y mm	Ultimate load P_u kN	Ultimate load deflection Δ_u mm
NS1	42	1.473	45	1.47	265.1	10.93	320	14.60
HS1	67	0.491	45	2.23	132.5		178	25.45
HS2	70	0.842	54	1.58	185.6	10.47	249	17.56
HS7	74	1.193	54	1.45	216.9	8.09	356	17.00
HS3	69	1.473	63	1.38	272.7	8.84	356	13.10
HS4	66	2.245	–	–	286.6	8.99	418	14.74
NS2	30	0.944	54	1.20	266.9	7.20	396	13.07
HS5	68	0.640	–	–	260.5	8.04	365	16.90
HS6	70	0.944	63	1.10	355.8	8.40	489	14.90
HS8	69	1.067	63	1.03	279.3	6.69	436	13.10
HS9	74	1.547	63	1.09	402.7	7.88	543	10.80
HS10	80	2.240	80	1.06	606.4	9.40	645	9.86
HS11	70	0.889	–	–	110.9	8.57	196	27.00
HS12	75	1.422	36	2.22	144.2	9.65	258	26.30
HS13	68	1.867	45	2.21	251.4	14.82	267	16.15
HS14	72	1.473	72	1.53	292.4	8.27	498	17.80
HS15	71	1.473	–	–	359.6	8.69	560	20.80

Series I slab. That effect is proportional to the square of the slab effective depth.

Slabs NS1 and HS3 (Series I), NS2 and HS6 (Series II) were made with different concrete strength, and had the same reinforcement ratio. Fig. 5.1 indicates that for any given load, the deflection of the normal strength concrete slabs were slightly greater than those made with high-strength concrete. This shows that the slab stiffness increased with the concrete strength but at a rate less than the ratio of the square roots of f'_c. As expected, the slab stiffness increased as the column size was increased as seen in Series IV test results, presented in Table 5.2.

In these tests the slab corners were free to lift, as would occur in an actual flat plate system (once cracking started the points of contraflexure no longer remains constant). In general, the slab corner lift-off for test slabs was about 20 % of the downward maximum deflection and occurred at about 40 % of the ultimate load.

5.3 Ductility and Energy Absorption

Ductility is quantified in terms of the ratio of the deflection at the ultimate load to the deflection at the first yielding of flexural reinforcement. The energy absorption is defined as the area under the load deflection curve. The ductility at failure and the energy absorption capacity of all the slabs are shown in Table 5.2.

Within a given series, the ductility decreased as the reinforcement was increased. For example, increasing the reinforcement ratio, in Series I slabs, form 1.193 % to 2.245 % decreased the ductility by 22 %. While for Series II, the ductility decreased by 46 % when the reinforcement ratio was increased from 1.067 % to 2.240 %. Ductility was less for Series II than for Series I. That result demonstrates a decrease in ductility with increasing shear effect as the slab depth is increased.

Table 5.2: Observed ductility and stiffness

Slab No.	Concrete strength f'_c MPa	Steel ratio ρ %	Ductility $\frac{\Delta_y}{\Delta_u}$ μ	Stifness kN/mm	Energy absorption Capacity kN.mm $*10^3$
NS1	42	1.473	1.34	21.49	2.6
HS1	67	0.491	–	–	3.6
HS2	70	0.842	1.68	11.95	2.7
HS7	74	1.193	2.10	23.90	–
HS3	69	1.473	1.48	28.08	2.6
HS4	66	2.245	1.64	31.40	3.3
NS2	30	0.944	1.56	28.52	4.0
HS5	68	0.640	2.10	19.26	4.1
HS6	70	0.944	1.79	37.60	4.3
HS8	69	1.067	1.96	37.70	3.4
HS9	74	1.547	1.37	49.42	3.4
HS10	80	2.240	1.05	66.28	3.6
HS11	79	0.889	3.15	7.30	3.6
HS12	75	1.422	2.73	13.08	3.4
HS13	68	1.867	1.09	17.20	2.6
HS14	72	1.473	2.15	31.77	5.1
HS15	71	1.473	2.39	32.49	7.2

Ductility is slightly increased with the increase in concrete strength. Increasing the column size, increased the ductility as seen from Series IV slabs, presented in Table 5.2.

The energy absorption of the slabs is decreased as the reinforcement increased. Slabs failing in flexure showed a higher energy absorption capacity than those failing in shear. Also, as the slab depth is decreased, energy absorption increased. The effect of concrete strength on the energy absorption capacity was not a significant factor, as an increase in the concrete strength resulted in a slight increase in the energy absorption capacity of the test slab.

5.4   Slab Rotation

Observed angles of rotation at failure ψ are given in Table 5.3. The relation between the observed values of the angle of rotation of the slab portion outside the shear crack and the load P is presented in Figs. 5.3 and 5.4. The slab rotation decreased with increasing the reinforcement ratio and the concrete strength.

5.5   Concrete Strains

The concrete strains were measured at different locations as mentioned in sec 4.3.4. For all the test slabs, measurements were made to determine the distribution of the concrete strain along a radius of the slab.

Fig. 5.5 presents the strain distribution along a radius of the slab. The radial strains were high at the column face but they decreased rapidly as the radius increased as shown in Fig. 5.5. In some cases, prior to failure, the radial strains at the column face started to decrease. As seen from Fig. 5.5, the strains in the

Table 5.3: Deformation characteristics of test slabs

Slab No.	Concrete strenght f'_c	Steel ρ	Ultimate steel strain $\epsilon_{su} * 10^3$	Ultimate concrete strain				Ultimate rotation $\psi * 10^3$	Radius of yield mm
				Radial		Tangential			
				mid $\epsilon_{cr} * 10^3$	corner $\epsilon_{cr} * 10^3$	mid† $\epsilon_{ct} * 10^3$	corner‡ $\epsilon_{ct} * 10^3$		
NS1	42	1.473	3.13	–	–	2.24	–	11.8	304
HS1	67	0.491	13.90	–	–	–	–	–	–
HS2	70	0.842	3.10	1.17	–	–	–	18.4	512
HS7	74	1.193	3.79	–	–	2.09	–	15.5	381
HS3	69	1.473	2.92	1.70	–	–	–	12.4	252
HS4	66	2.245	3.09	2.90	–	–	–	12.4	213
NS2	30	0.944	–	–	–	–	–	11.1	–
HS5	68	0.640	3.56	1.29	–	–	–	13.6	–
HS6	70	0.944	3.22	–	–	2.40	2.95	12.2	–
HS8	69	1.067	4.15	–	–	2.36	2.92	12.3	452
HS9	74	1.547	2.96	–	–	2.04	2.82	9.7	344
HS10	80	2.240	2.54	–	–	1.97	1.49	11.1	–
HS11	70	0.889	6.84	–	–	1.63	1.70	–	658
HS12	75	1.422	3.66	–	–	1.83	2.36	21.2	371
HS13	68	1.867	3.70	–	–	2.33	2.78	13.9	362
HS14	72	1.473	3.35	–	–	1.72	2.89	18.6	–
HS15	71	1.473	4.69	–	–	1.71	2.02	21.6	–

† Gauge G1, Fig. 5.6

‡ Gauge G2, Fig. 5.6
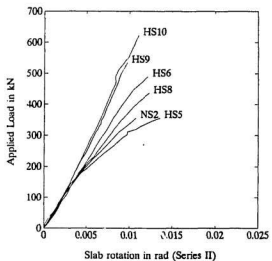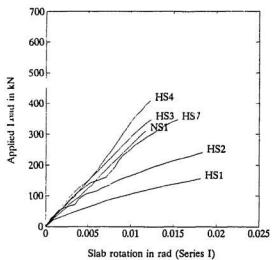
Figure 5.3: Typical load-rotation characteristics in the lateral direction for test slabs (Series I and II)
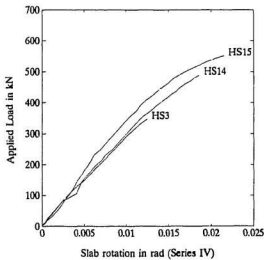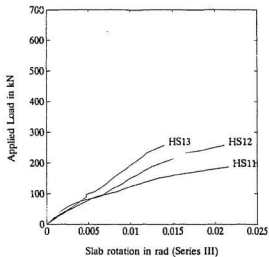
Figure 5.4: Typical load-rotation characteristics in the lateral direction for test slabs (Series III and VI)

tangential direction have smaller gradients $d\epsilon_{ct}/dr$ than those in the radial direction and with good approximation these tangential strains can be assumed inversely proportional to the radius as proposed by Kinnunen and Nylander [27].

The strains on the radii through the corners of the column stub (gauge G2. Fig. 5.6) were higher than those at the middle of the column face (gauge G1 in Fig. 5.6), and in some cases they reached a value of 0.003 in the loading step prior to failure. This indicates a concentration of stress at the corners of the column stub. Fig. 5.6 presents the load versus strain measured at these two different positions. Neither the concrete strains in the tangential nor the radial direction reached a limiting value of 0.0035 for any of the tested slabs.

Unfortunately, in the normal strength concrete reference slabs, some of the strain gauges around the column were damaged during testing and hence it was not possible to compare the strains for the normal strength and high-strength concrete slabs.

It is worth mentioning here that while the concrete strain gauges readings gave some indication of the crack formation in the slab, these gauges were damaged after the cracks started forming.

5.6 Steel Strains

In order to obtain information on the state of stress in the flexural reinforcement of the test slabs, the strain in the this reinforcement was measured at points of special interest, as mentioned in sec 4.4.3. For all the tested slabs, measurements were made to determine the strain distribution along a radius. According to the experimentally obtained stress-strain curve of the reinforcement, the yield strain of a steel bar
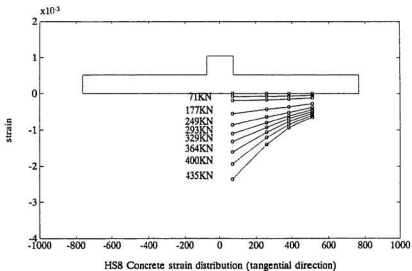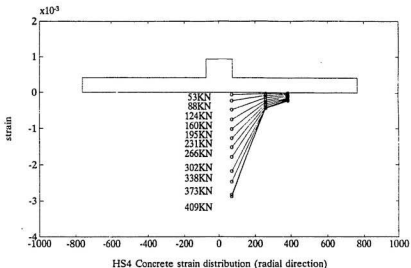
Figure 5.5: Observed distribution of the concrete strain, ϵ_c, at the top of test slabs HS4 and HS8 at various values of the load P (kN)
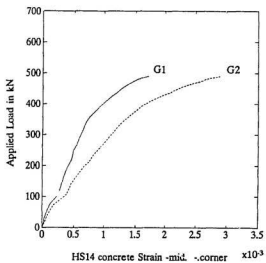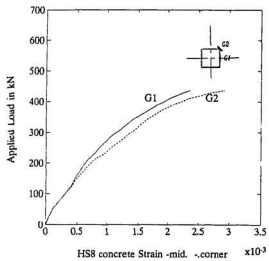
Figure 5.6: Applied load versus concrete strain around the column periphery

reached 2500 microstrains. The highest strains and consequently initial yielding occurred below the stub-column. In all the tested slabs, the tension reinforcement yielded before punching took place. The degree to which yielding spread in the reinforcement varied with the reinforcement ratio. At high reinforcement levels, the yield of tension reinforcement occurred at high loads and was localized at the column stub. For lightly reinforced slabs, yielding initiated at the column stub and gradually progressed throughout the whole tension reinforcement. The observed values of the radius of yield r_y, which normally determine the extend of yielding of reinforcement in the slab, are given in Table 5.3.

Fig. 5.7 presents the strain distribution along a radius of the slab. As seen from these graphs, the strain in the flexural reinforcement can with good approximation be assumed inversely proportional to the slab radius.

Typical curves representing the relation between the observed values of strain in the flexural reinforcement at the column, and the applied load are shown in Figs. 5.8 and 5.9.

5.7 Cracking Characteristics

Cracking patterns at failure are shown in Figs. 5.10 through 5.14. For slab HS1, the crack pattern observed prior to punching consisted of one tangential crack roughly at the column outline followed by radial cracking extending from the column. Yet, befo e the flexure yield lines were well developed, punching failure occurred. This failure can be classified as flexure-punching or secondary shear failure.

The initial flexural cracks recorded for all the test slabs were first formed tangentially under the edge of the column stub, followed by radial cracking extending

HS3 Steel strain distribution

HS9 Steel strain distribution
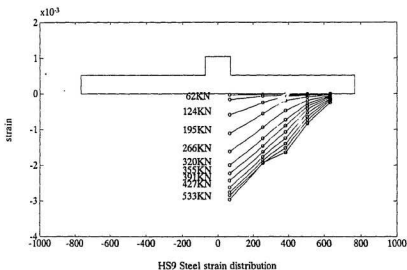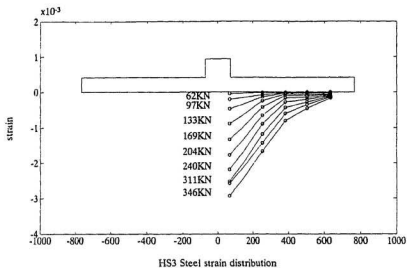
Figure 5.7: Observed distribution of the strain in the flexural reinforcement, ϵ_s, at for test slabs HS3 and HS9 at various values of the load P (kN)
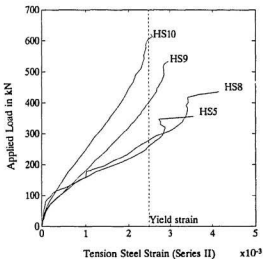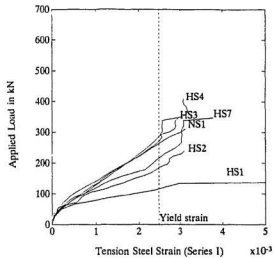
Figure 5.8: Typical load-tension steel strain behaviour at the column periphery for test slabs (Series I and II)
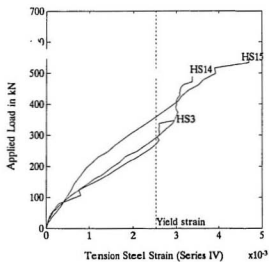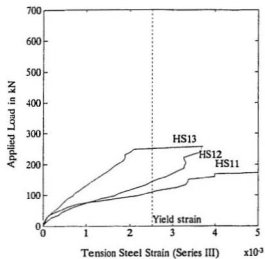
Figure 5.9: Typical load-tension steel strain behaviour at the column periphery for test slabs (Series III and VI)
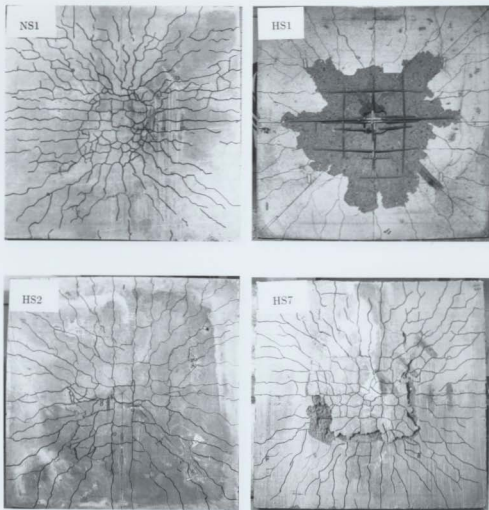
Figure 5.10: Failure patterns of test slabs NS1, HS1, HS2 and HS7
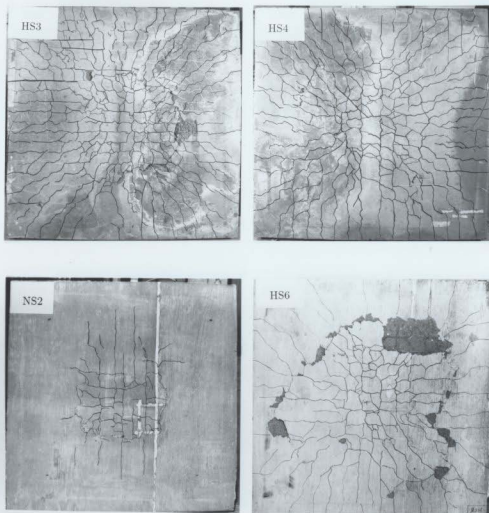
Figure 5.11: Failure patterns of test slabs HS3, HS4, NS2, and HS6
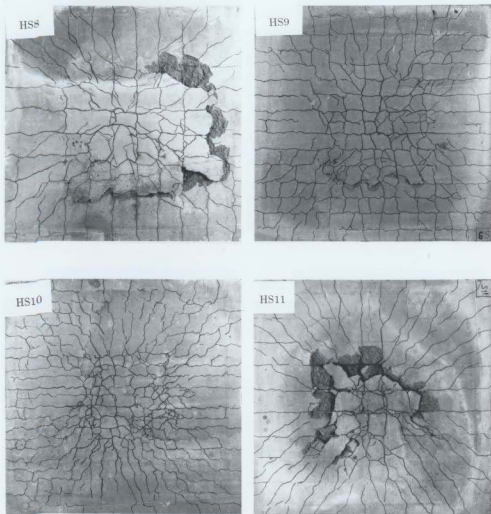
Figure 5.12: Failure patterns of test slabs HS8, HS9, HS10, and HS11
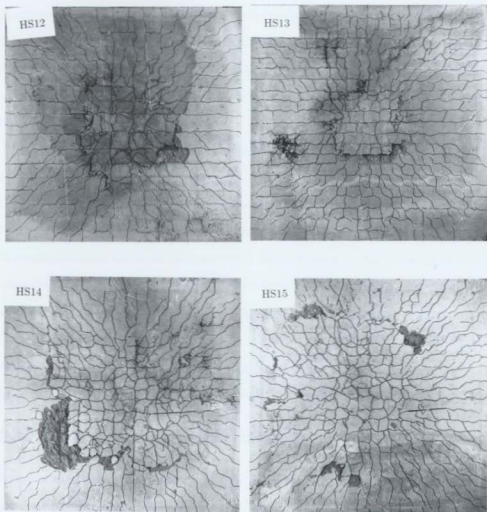
Figure 5.13: Failure patterns of test slabs HS12, HS13, HS14, and HS15

from the column. The first radial cracks were much more pronounced along lines parallel to the reinforcement crossing through the column stub. As the load was increased, the tangential cracks were then extended outside the circumference of the stub column. It is worth mentioning here that those tangential cracks were limited to the column vicinity. The slabs failed with the final shear crack coinciding with, or located outside this cracks. Final failure developed by the column punching through the slab.

It was not possible to determine a reliable value for the shear cracking load, i.e. the load at which the shear cracks began to open up. The estimation of such load from the crack pattern was uncertain because there was no fundamental difference between the shear cracks and flexural cracks running in a tangential direction. Moreover, because the slabs were provided with two-way reinforcement, the initial shear crack might have remained above the level of reinforcement, in which case it would not become visible on the tensile face of the slab. However, as proposed by Kinnunen and Nylander (1960), utilizing the decrease of the strains in the flexure reinforcement as a guide for determining the shear cracking loads, the observed loads were always greater than 70 - 80 % of the ultimate load.

5.8   Post Punching Behaviour

Post punching behaviour was monitored in some of the tests. When punching occurred the load fell suddenly to a value of 20 % of the ultimate load and was released completely in some cases. With further application of the load, a flat plateau of resistance was reached. The final failure progressed with the bottom bars being pulled out of the concrete.

5.9 Modes of Failure

All the test specimens, except HS1 and HS11, failed in shear. Slabs HS2, HS7, HS6, HS8 and HS12 showed a ductile punching failure with the slabs failing before the flexure strength was exceeded. The test slab HS5 had a low reinforcement ratio (ρ = 0.64 %) and was designed to fail in flexure, but both the load deflection curve and the strain distribution of this slab indicated that the slab exhibited a gradual and ductile punching failure. The rest of the slabs, namely; HS3, HS4, HS9, HS10 and HS13 clearly failed in pure punching long before their flexure strength was reached.

The punching shear surface on the tension face occurred at a distance of (1.2 - 1.6) times the slab depth (d) from the column face for most of the test slabs. The failure surface of few of the test specimens were carefully removed and examined. The observed angles of failure surface varied considerably. For normal strength concrete slabs, NS1 and NS2, this angle was found to be between 26 and 30 deg, in agreement with other test data [39], while for high-strength concrete slabs the observed angle of failure surface varied between 32 - 38 deg.

As expected, the ultimate punching shear load increased as the reinforcement ratio was increased. Also, increasing the compressive strength increased the ultimate punching load but at a rate less than squre root of the slab compressive strength.

5.10 Test Results versus Codes Predictions

The shear and flexural behaviours of the slab-column connection region are known to be very strongly interrelated. The ratio of the observed strength prior to punch-

ing to that computed by the yield line, Φ_o, has often been used to divide punching failures into shear failure ($\Phi_o \leq 1$) and flexural failure ($\Phi_o > 1$).

The flexural ultimate load capacity of two-way slabs can be calculated from yield-line theory. The yield-line pattern giving the minimum load for conventional slab-column specimens is shown in Fig. 5.15. The flexural punching load required for this mechanism is

$$P_{flex} = K M_b \tag{5.1}$$

From consideration of the virtual work done by the actions on the yield lines, the solution for this mechanism is

$$K = 8\left(\frac{s}{a-c} - 0.172\right) \tag{5.2}$$

M_b is calculated from the widely accepted equation proposed by the American Concrete Institute (ACI)

$$M_b = \rho f_y d^2 (1 - 0.59 \rho f_y / f'_c) \tag{5.3}$$

The ACI 318 (1983) [48] and CSA (CAN3-A23.3-M84) [49] codes are based mainly on Moe's work [25], while the BS 8110 (1985) [50] codes is based on Regan's work [51]. These present building codes specifications for shear strength of reinforced concrete slabs are based on the test results of slabs made with relatively low compressive strengths, varying mostly from 14 to 40 MPa. Hence, it is necessary to re-examine the present shear design methods when applied to high-strength concrete.

The current ACI 318 (1983) code provisions, when expressed at the column face and with a capacity reduction factor of unity, become

$$v_u = \frac{P_u}{4cd} = 4\left(1 + \frac{c}{d}\right)\sqrt{f'_c} \tag{5.4}$$
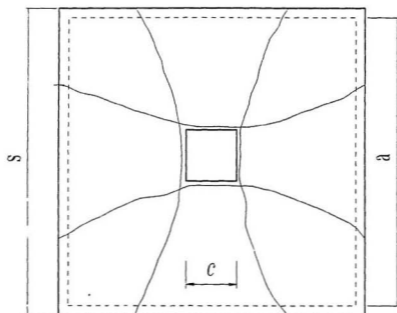
Figure 5.14: Yield line mechanism

These code provisions are derived mainly from the following expression proposed by Moe [25]

$$v_u = \frac{P_u}{cd} = \frac{15(1 - \frac{0.075}{d})\sqrt{f'_c}}{1 + \frac{5.25bd\sqrt{f'_c}}{P_{flex}}} \quad (5.5)$$

Provided that $\Phi_o \leq 1$

The square root expression was adopted by Moe [25] who concluded that the shear failure is controlled primarily by the tensile splitting strength which is assumed proportional to $\sqrt{f'_c}$.

The ultimate recorded test loads are given in Table 5.4 together with the details of the specimens and the results of comparisons with the values estimated by different codes. The limit of 40 MPa of the maximum useful cube strength has been ignored while applying CP 110 (1972) and BS 8110 (1985). ACI 318 (1983) code was applied with capacity reduction value ϕ omitted.

It is clear from Table 5.4 that Moe's equation (Eq. 5.5) overestimates the punching shear capacity of high-strength concrete, and in the case of HS2 it overestimated the punching load by 44 %. Different codes equations seems to be slightly conservative in predicting the punching loads.

The use of the square root of the concrete strength as given in the ACI 318 code (1983) Eq. 5.4, also appears to over-estimate the influence of this parameter. Both the American ACI 318 (1983) and Canadian CAN3-A23.3-M84 (1984) codes neglect the contribution of reinforcement as an influential parameter for the two way shear capacity of the slabs. This produces a difference in the ratios of the calculated and experimental ultimate loads for the slabs made with different steel ratios and same concrete strength. The British standards gives a better estimate for the punching

Table 5.4: Comparison of code predictions with test results

Slab No.	f'_c MPa	ρ %	P_u kN	P_{code}/P_u				$\dfrac{P_u}{P_{flex}}$
				BS 8110	CP 110	ACI 318-83	Moe	
NS1	42.0	1.474	320.	0.85	0.80	0.63	0.95	0.63
HS1	67.0	0.491	178.	1.24	1.17	1.42	1.78	0.96
HS2	70.2	.842	249.	1.08	1.02	1.04	1.44	0.80
HS7	73.8	1.193	356.	0.86	0.81	0.75	1.02	0.81
HS3	69.1	1.474	356.	0.90	0.85	0.72	1.07	0.67
HS4	65.8	2.370	418.	0.82	0.79	0.56	0.86	0.63
NS2	30.0	0.944	400.	0.73	0.64	0.59	0.79	0.76
HS5	68.1	0.640	365.	0.98	0.84	0.93	1.27	0.88
HS6	70.0	0.944	489.	0.80	0.69	0.74	0.92	0.88
HS8	69.0	1.111	436.	0.94	0.82	0.82	1.10	0.74
HS9	74.0	1.611	543.	0.87	0.76	0.68	0.97	0.65
HS10	80.0	2.333	645.	0.85	0.74	0.60	0.89	0.54
HS11	70.0	0.952	196.	0.94	0.87	0.87	1.07	1.03
HS12	75.0	1.524	258.	0.85	0.79	0.69	0.94	0.86
HS13	68.0	2.000	267.	0.87	0.81	0.63	0.96	0.70
HS14	72.0	1.474	498.	0.76	0.72	0.68	0.92	0.88
HS15	71.0	1.474	560.	0.78	0.74	0.75	0.94	0.92

load. The BS 8110 (1985) and CP110 (1972) assumption that punching resistance is proportional to the cubic root of the concrete compressive strength can be seen to be more reasonable.

Chapter 6

PROPOSED MECHANICAL MODEL

6.1 Introduction

The experimental program carried out on the seventeen concrete slabs has provided the basis for the proposed model. Test results revealed that the Kinnunen and Nylander rational model still provides the best account of the punching behaviour of concrete slabs. In the present chapter, a modification and adaptation for the use of this model for high-strength concrete slabs is presented.

6.2 Punching Failure Mechanism

The slab is divided into rigid radial segments, each bounded by two radial crack lines, a part of the initial circumferential crack and the slab boundary, as illustrated in Fig 6.1. The radial segment rotates around a centre of rotation (C.R.) located at the face of the column and on the level of the neutral axis, as proposed by Shehata and Regan [40]. This idealized model allows the deformation of the part of the slab which is on the top of the column and bounded by the shear crack.

Thus, the dowel forces can be directly calculated from the model equilibrium. In Kinnunen and Nylander's model, this portion of the slab was considered to remain undeformed in contradiction to test results and the dowel forces had an established value of 30 % of the ultimate load.

The angle of the shear crack is hard to determine experimentally. However, the angle of inclination of the failure surface can be measured. The observed angle of the failure surface of high-strength concrete slabs varied between 32 and 38 deg while the angle ranged between 26 and 30 deg for normal strength concrete, as mentioned in sec 5.8. The assumed relation between the average angle of failure surface and the inclination of the shear crack is illustrated in Fig 6.2.

The part of the slab between two radial cracks is assumed to rotate as a rigid body between the slab edge and the column perimeter. On the basis of this assumption, the concrete and steel strains can be calculated as a function of the tangential curvature of the slab as shown in Fig 6.3. Hence, the tangential steel strain ϵ_{ct} and the steel strain ϵ_s at a distance r from the centre of the slab can be calculated from the following expressions

$$\epsilon_{ct} = \psi \frac{x}{r}, \tag{6.1}$$

and

$$\epsilon_s = \psi \frac{d-x}{r} \tag{6.2}$$

SECTOR ELEMENT

INCLINED SHEAR CRACK

x
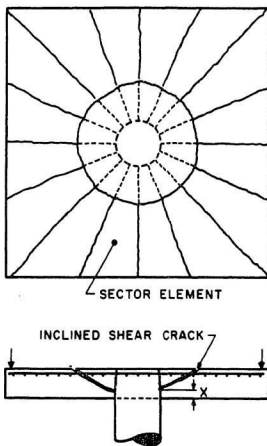
Figure 6.1: Modified Kinnunen and Nylander punching model.
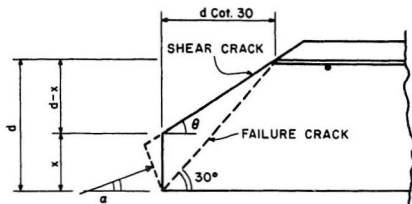
Figure 6.2: Failure crack and assumed shear crack.
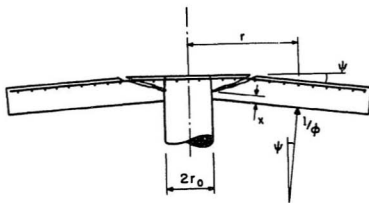
Figure 6.3: Relation between deformations and strains.

6.3 Stress-Strain Relationships

The stress-strain curve for the reinforcement is assumed to be ideally elasto-plastic with the yield strain ϵ_{sy}, as shown in Fig 6.4

$$\epsilon_{sy} = \frac{f_y}{E_s} \tag{6.3}$$

The concrete stress strain curves are also assumed to be elasto-plastic, with the yield strain ϵ_{c1} and ultimate strain ϵ_{cu} as shown in Fig 6.4. The concrete's modulus of elasticity E_c is equal to

$$E_c = 4700\sqrt{f_c'} \quad \text{(MPa)}$$

6.4 Forces Acting on a Radial Segment

The forces on a radial segment (Fig 6.5) can be summarized as follows:

1. The external load or (reaction) $P\Delta\Phi/2\pi$,

2. Tangential forces in the steel crossing the radial cracks, dF_{st}.

3. Radial forces in the steel crossing the inclined crack, dF_{sr}.

4. Forces in the concrete normal to the radial crack, dF_{ct}.

5. Forces in the concrete at the face of the column, dF_{cr}.

6. Dowel forces in the steel crossing the inclined crack, dD.
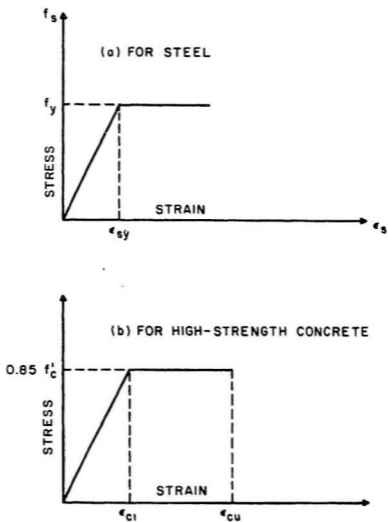
Figure 6.4: Idealized stress-strain curves for steel and concrete.
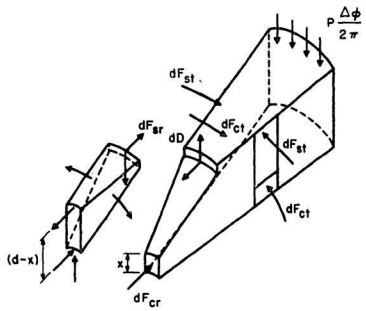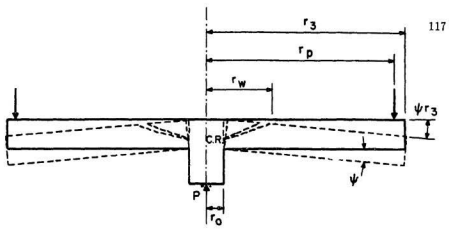
Figure 6.5: Punching failure model and forces.

6.4.1 Steel Forces

The idealized stress-strain curve for the reinforcing steel is shown in Fig 6.4. For an orthogonal mesh type of reinforcement, with the bars equally spaced in both directions, the effective radial and tangential steel ratios are assumed equal.

From the rigid body rotation, the radius within which all the flexural reinforcement yields (r_y) is

$$r_y = \psi \frac{d}{\epsilon_{sy}} (1 - \frac{x}{d})$$

while the punching radius (r_w), as illustrated in Fig 6.2, is equal to

$$r_w = r_o + d \cot 25°$$

The total tangential steel force acting on a radial segment can be calculated using the following expressions:

If the radius of yield is smaller than the punching radius, i.e. $r_y < r_w$, then

$$
\begin{aligned}
F_{st} &= \int_{r_w}^{r_3} \rho_t f_y d \, dr \\
&= \rho_t f_y d \, r_y \ln \frac{r_3}{r_w} \,,
\end{aligned}
\tag{6.4}
$$

and if the radius of yield is greater than the punching radius, i.e. $r_y \geq r_w$, then

$$
\begin{aligned}
F_{st} &= \int_{r_w}^{r_y} \rho_t f_y d \, dr + \int_{r_y}^{r_3} \rho_t f_y d \, dr \\
&= \rho_t f_y d \, [r_y - r_w] + r_y \ln \frac{r_3}{r_y} \,,
\end{aligned}
\tag{6.5}
$$

Similarly, the radial forces in the flexural reinforcement acting on the radial segment are given by

For $r_y < r_w$

$$dF_{sr} = \rho_r \, f_y \, d \, r_y \, \Delta\Phi \; , \tag{6.6}$$

and for $r_y \geq r_w$

$$dF_{sr} = \rho_r \, f_y \, d \, r_w \, \Delta\Phi \; . \tag{6.7}$$

The total radial steel forces acting on the segment is equal to

$$F_{stot} = F_{sr} \div F_{st} \, \Delta\Phi \tag{6.8}$$

6.4.2 Concrete Forces

Each radial segment is supported by an inclined compressive force, as shown in Fig 6.5. The magnitude of this force can be calculated from the maximum concrete bearing stress (Fig 6.6), and hence the ultimate concrete forces at the column face dF_{cr} can be calculated from the following expression

$$dF_{cr} = \sigma_{bu} \, f'_c \, A_c \; , \tag{6.9}$$

where σ_{bu}, the ultimate bearing strength of concrete, is given by

$$\sigma_{bu} = \sqrt{\frac{r_o + d}{r_o}} \; \leq 1.4 f'_c \tag{6.10}$$

and the bearing area at the column head, A_c, is

$$A_c = \Delta\Phi [r_o - \frac{x \sin(90 - \theta)}{2 \sin(90 + \theta - \alpha)}] \frac{x \sin(90 - \theta)}{\sin(90 + \theta - \alpha)} \tag{6.11}$$

The tangential concrete force acting on a radial element at radius r and thickness dr is

$$F_{ct} = K_c \, f'_c \, x \, dr \tag{6.12}$$
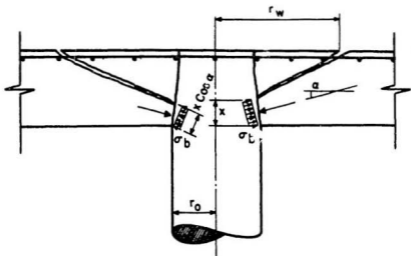
Figure 6.6: Bearing stress failure at the column face.

where K_c is a function that define the stress block according to the idealized stress-strain curve for concrete shown in Fig 6.4

$$K_c = \begin{cases} 0.425 \frac{\epsilon_c}{\epsilon_{c1}} & \text{for } \epsilon_c \leq \epsilon_{c1} \\ 0.85(1 - \frac{\epsilon_{c1}}{2\epsilon_c}) & \text{for } \epsilon_c > \epsilon_{c1} \end{cases}$$

Integrating Eq 6.12 from $r = r_o$ to $r = r_3$, gives the value of the tangential forces acting on a radial segment

$$F_{ct} = \int_{r_o}^{r_{\epsilon_c = \epsilon_{c1}}} K_c \, f_c \, x \, dr + \int_{r_{\epsilon_c = \epsilon_1}}^{r_3} K_c \, f_c \, x \, dr \tag{6.13}$$

From the rigid body rotation

$$r_{\epsilon_{c1}} = \psi \frac{x}{\epsilon_{c1}}, \tag{6.14}$$

Eq 6.13 now becomes;

For $r_o < r_{\epsilon_c = \epsilon_{cu}}$

$$\begin{aligned}
F_{ct} &= 0.425 \, f_c \, x^2 \, \frac{\psi}{\epsilon_{c1}} \ln \frac{\psi x}{r_3 \epsilon_{c1}} \\
&+ 0.85 \, f_c \, x(r_3 - \frac{\psi x}{\epsilon_{c1}})(1 - \frac{\epsilon_{c1}}{4\psi x}(r3 + \frac{\psi x}{\epsilon_{c1}}))
\end{aligned} \tag{6.15}$$

For $r_o \geq r_{\epsilon_c = \epsilon_{cu}}$

$$F_{ct} = 0.425 \, f_c \, x^2 \frac{\psi}{\epsilon_{c1}} \ln \frac{r_3}{r_o} \tag{6.16}$$

6.4.3 Dowel Forces

The dowel forces are calculated from the equilibrium of the wedge element shown in Fig 6.5

$$dD(r_w - r_o) = \rho_r \, d \, (\sigma_{s(r_w)} r_w - \sigma_{s(r_o)} r_o) + (\int_{r_o}^{r_w} \rho_t \, f_y \, d \, dr)\Delta\Phi \tag{6.17}$$

Hence the dowel forces can be calculated using the following expressions

For $r_y < r_w$

$$dD = \frac{d-x}{r_w - r_o} \, \rho_r \, f_y \, d \, r_y \, \ln \frac{r_w}{r_y} \, \Delta\Phi \, , \tag{6.18}$$

and for $r_y \geq r_w$

$$dD = 0 \, . \tag{6.19}$$

6.5 Calculation of the Ultimate Load

The three equilibrium equations in a radial plane are

$$dF_{cr} \, \cos \, \alpha + F_{ct} = dF_{sr} + F_{st}\Delta\Phi \tag{6.20}$$

$$P \, \frac{\Delta\Phi}{2\pi} = dF_{cr} \, \sin \, \alpha \, + dD \tag{6.21}$$

$$P \, \frac{\Delta\Phi}{2\pi} \, (r_p - r_o) = (dF_{sr} + dF_{st} \, \Delta\Phi)z \, + dD(r_w - r_o) \tag{6.22}$$

where z is the lever arm and is equal to $(d - 0.45x)$.

By solving these three non linear equations, the angle of rotation ψ, the neutral axis depth x and the inclination of the compressive forces at the column face α, can be determined.

6.6 Failure Criteria

Failure is assumed to occur when one of these criteria are satisfied:

1. if the yielding of tension reinforcement is reached in the whole slab.

2. If the tangential strain at the column periphery reaches a characteristic value of 0.0035;

$$\epsilon_{ct} = \psi \frac{x}{r_o} \leq 0.0035 \tag{6.23}$$

6.7 Numerical Procedure

This algorithm is designed to solve the basic equilibrium equations ($\Sigma x = 0$, $\Sigma y = 0$ and $\Sigma M = 0$) of a typical radial segment. These three nonlinear equations are given by Equations 6.20, 6.21 and 6.22 as mentioned earlier. The unknowns in these equations are P, x, α, and ψ. The numerical procedure starts by assuming an angle of rotation ψ. Once the angle of rotation ψ is assumed, the three equilibrium equations will provide a solution for the three unknowns values P, x, and α as follows:

1. Assume an angle of inclination (α) for the compressive force at the column face.

2. Determine the location of the neutral axis (x) by satisfying the condition that the total steel forces are equa' to the total concrete forces as expressed in Eq. 6.20.

3. Using Eq. 6.22, find the value of P.

4. Determine a second value for the angle (α) from Eq. 6.21.

5. Compare the assumed (α) from step (1) with the calcula.ed alpha from step (4). If they are equal, it means that this is the correct angle of inclination for the compressive force at the column face. If the two angles are not equal, repeat the iteration cycle from step (1) to (3) till conversion is accomplished.

After the correct values of P, x, and α are determined for the assumed rotation angle ψ, the failure criteria must be checked. At failure, the tangential strain at the

column head will reach a limiting value of 0.0035 as expressed in Eq. 6.23. Several angles of rotation ψ are assumed and the entire numerical cycle will be repeated until the failure criteria is satisfied. A computer program was developed based on the above procedure to determine the values of P, ψ, x, and α at failure.

6.8 Comparison of Test Results with the Assumed Theoretical Model

A comparison of test results to the proposed model is shown in Table 6.1. The proposed model provides better results, when compared with Kinnunen and Nylander's model [27] and Shehata and Regan's model [40]. The model was also used to predict the punching capacity of normal strength slabs tested by Elstener and Hognestad [24], Kinnunen and Nylander [27], and Kinnunen, Nylander and Tolf [53]. The results are shown in Tables B1 through B3 of Appendix B.

The proposed model yields a more accurate prediction of the punching capacity of concrete slabs in general and high-strength concrete in particular. Although the proposed model utilizes Shehata and Regan's [40] improvement of the original Kinnunen and Nylander's model by allowing the deformation of the portion of the slab which is on the top of the column and bounded by the shear crack, the proposed model does not recognize the stress gradient at the failure zone nor the lateral splitting of concrete as assumed by Shehata and Regan. Rather, it assumes that the bearing capacity reaches a limiting value at the column face.

The experimental evidence indicated that the failure is localized at the column face and does not occur over the whole front panel at the column face. Therefore, the restricted crushing nature of the concrete at the column face indicates a direct

Table 6.1: Comparison of theoretical results with test results

Slab no.	d, mm	Column size, mm	r_3, mm	ρ, %	f'_c, MPa	f_y, MPa	$\dfrac{P^1_{calc}}{P_{test}}$	$\dfrac{P^2_{calc}}{P_{test}}$	$\dfrac{P^3_{calc}}{P_{test}}$
NS1	95	150	1500	1.47	42.0	490	0.79	1.04	0.94
HS1	95	"	"		70.0	"	0.89	0.94	0.92
HS2	95	"	"	0.84	70.0	"	0.92	1.05	1.04
HS7	95	"	"	1.19	74.0	"	0.79	0.94	0.92
HS3	95	"	"	1.47	69.0	"	0.85	1.04	1.03
HS4	90	"	"	2.37	66.0	"	0.78	0.94	0.92
HS5	120	"	"	0.64	68.0	420	1.05	1.02	0.99
HS8	120	"	"	1.11	69.0	490	1.11	1.15	1.04
HS9	120	"	"	1.61	74.0	420	1.15	1.23	1.06
HS10	120	"	"	2.33	80.0	"	1.21	1.33	1.10
HS11	70	"	"	0.95	70.0	"	0.68	0.70	0.78
HS12	70	"	"	1.52	75.0	"	0.68	0.70	0.81
HS13	70	"	"	2.00	68.0	"	0.71	0.76	0.84
HS14	95	220	"	1.47	72.0	"	0.85	0.85	0.97
HS15	95	300	"	1.47	71.0	"	0.96	0.87	0.99

[1] Kinnunen and Nylander (1960)
[2] Shehata and Regan (1989)
[3] Proposed model

bearing failure. Test results also showed that the concrete strain measurements in the radial direction never reached the values recommended by Shehata and Regan. Although the radial strains sometimes exceed the tangential strains a. the column face, this occurs at locations very close to the column face and extends over a short distance. Near failure, the .adial strains tends to decrease as observed experimentally.

The proposed model did not assume any limiting value of the angle of inclination of the compressive force at the column face (α), as in Shehata and Regan's model. Nevertheless, the angle α must be established from the model equilibrium as explained earlier. According to the finite element analysis carried out by Shehata [39], the limiting value of $\alpha = 20°$, may only be true for the elastic analysis. However, near failure, the concrete adjacent to the column head is far from elastic. Thus the assumption of a limiting value of $\alpha = 20°$ and consequently the occurence of maximum stresses would not be valid close to failure.

Chapter 7

Conclusions

The present research investigation was carried out in three stages, viz., material investigation, experimental tests on slab and a rational model to predict the ultimate capacity of the test slabs. The material part involved the development of a high-strength concrete mix, suitable for offshore applications. The basic mechanical properties were examined. In addition, an experimental program was carried out to study the effect of cold ocean water, simulated under laboratory conditions, on the mechanical properties of green high-strength concrete containing silica fume and fly ash. The experimental test carried out on two way slabs included the study of the structural behaviour and strength characteristics of seventeen two-way slabs made with high-strength and normal strength concrete subject to punching shear. In addition, a mechanical model based on the test results, strain compatibility and equilibrium equations was proposed. The following conclusions can be drawn from the present research:

7.1 Material Investigation

The following conclusions may be reached from the present investigation concerning the effect of cold ocean water on high strength concrete specimens cured for 24 hours at room temperature and exposed for 91 days.

1. It was possible to produce high strength concrete with the use of rich mix, 12% fly ash, 8% silica fume replacement of cement, and low water cement ratio using local aggregates and cement. The average compressive strength after 28 days was about 70 MPa.

2. The compressive strength was affected by the low temperature exposure more than the modulus of elasticity. The rate of maturity was reduced with the decrease of temperature. However, the compressive strength increased with the increase in exposure time.

3. The empirical formula suggested by ACI Committee 363, for evaluating the modulus of elasticity, gave good agreements with the test results, when it was applied to low temperature exposures as well as to room temperature exposure.

4. The modulus of elasticity was slightly affected by the increase of exposure time and it decreased with the decrease of exposure temperature.

5. The characteristic shape of the stress-strain curve for high strength concrete containing silica fume and fly ash was found to be similar to other high strength portland cement concrete. The recorded ultimate strain ranged between 0.0036 at the room temperature to a value of 0.00295 at a temperature

of $-10^\circ C$.

6. Severe surface deterioration was evident in all specimens exposed to cold ocean temperature of $-10^\circ C$ after 24 hours of room temperature curing. The deterioration was observed after 28 days of exposure and it can be explained to a combination of sulphate attack and ice damage.

7.2 Structural Investigation on the Two-way Slabs

Tests on seventeen concrete slabs were conducted and the results obtained have been presented and discussed in detail. Extensive measurements were carried out to determine the slabs deformations, strains, cracking characteristics and modes of failure. From the present investigation the following conclusions were reached:

1. The two main modes of punching failure of high-strength concrete slabs may be classified as flexure-punching and shear punching. However, high-strength concrete slabs exhibit a gradual and ductile punching failure at relatively low reinforcement ratios ($\rho = 0.64$).

2. As the reinforcement increased the stiffness increased. On the other hand the ductility decreased as the reinforcement increased.

3. The slab ductility slightly increased with increase in concrete strength.

4. The slab stiffness increased with the increase of the concrete strength but at a rate less than the ratio of the square root of f'_c.

5. The concrete strains recorded at the compressed face did not develop an entirely consistent value at failure. Nevertheless, these strains reached the

highest values adjacent to the column. The strains in the radial direction decreases very rapidly with increasing distance from the column.

6. The strains at the corner of the column were higher than those at the middle of the column indicating a higher stress concentration at the column corner.

7. When punching occurred, the load fell suddenly to 20 - 25% of the ultimate load and a flat plateau of resistance was reached

8. The observed angle of failure surface of high-strength concrete slabs varied between 32 - 38 deg compared with 26 - 30 deg for normal strength concrete.

9. The use of the square root of the concrete strength as given in the present North American Codes, over-estimates the influence of this parameter on the punching shear capacity of two-way slabs.

10. Moe's (1961) equation can't be applied to predict the punching shear capacity of high-strength concrete.

11. The British codes (CP110 and BS8110) assumption that punching resistance is proportional to the cubic root of the concrete compressive strength gives a better prediction of the punching shear of high-strength concrete slabs. It provided a consistent results when compared with the experimental results.

12. Based on the strain measurements and test results, a mechanical model was developed to predict the ultimate capacity of high-strength two-way slabs. The model uses the strain compatibility and equilibrium equations of an assumed failure criteria. A new formulations for the concrete and steel forces were developed. In addition, a new assumed failure criteria is proposed; failure

is assumed to occur if the strains at the column preiphery reached a charac-
teristic value of 0.0035. The ultimate bearing strength at the column head
does not recognize the lateral splitting of concrete as assumed by Shehata and
Regan. Rather, it assumes a local bearing type of failure at the coulmn head.
The proposed model provided good agreement with test results. Also, it gave
a better prediction of the ultimate loads than Kinnunen and Nylander, and
Shehata and Regan's proposed models.

References

[1] C. G. Hoff, "The Challenge of Offshore Concrete Structures," *Concrete International*, Vol. 7, No. 8, August 1985, pp. 12-22.

[2] H. Ronneberg and M. Sandvik, "High-Strength Concrete for North Sea Platforms," *Concrete International*, Vol. 12, No. 1, 1990, pp. 29-34.

[3] O. E. Gjorv, "Long-time Durability of Concrete in Sea Water," *Journal of the American Concrete Institute*, Vol. 68, 1971, pp. 60-67.

[4] P. K. Mehta, "Durability of Concrete in Marine Environment - A Review," *SP-65 Concrete in Marine Environment,* American Concrete Institute, Detroit, 1980, pp. 1-20.

[5] K. Mather, "Concrete Weathering at Treat Island, Maine," *SP-65 Concrete in Marine Environment,* American Concrete Institute, Detroit, 1980, pp. 101-112.

[6] P. K. Mehta and H. Haynes, "Durability of Concrete in Seawater," *Journal of the Structural Division*, Proceedings of the American Society of Civil Engineering, Vol. 101, ST 8, August 1975, pp. 1679-1686.

[7] ACI Committee 357, "Guide for Design and Construction of Fixed Offshore Structures," American Concrete Institute, Detroit, September 1985.

[8] Federation International de la Precontrainte, "Design and Construction of Concrete Sea Structures," London, Telford, 1985, fourth edition.

[9] J. Moskens and B. Jakobsan, "High-Strength Concrete Development and Potentials for Platform Design," *Offshore Technology Conference*, Paper OTC 5073, May 1985, pp. 485-497.

[10] A. K. Haug and M. Sandvik, "Mix Design and Strength Data for Concrete Platforms in the North Sea," *SP-109 Concrete in Marine Environment*, American Concrete Institute, Detroit, 1988, pp. 896-906.

[11] P. K. Mehta, "Durability of Concrete Exposed to Marine Environment - A Fresh Look," *SP-109 Concrete in Marine Environment,* American Concrete Institute, Detroit, 1988, pp. 1-29.

[12] "Supplementary Cementing Materials for Concrete," edited by V. M. Malhotra, CANMET Publ. SP 86-8E, 1987, 428 p.

[13] P. T. Seabrook and H. S. Wilson, "High-Strength Semi Light Weight Concrete for Use in Offshore Structures: Utilization of Fly Ash and Silica Fume," *Proceedings, CSCE/CANMET International Workshop on Concrete for Offshore Structures;* St. John's, Newfoundland, Canada, September 1986, 29 p. Available from CANMET, Energy, Mines and Resources, Ottawa, Canada.

[14] C. Bedard, G. Carette, and V. Malhotra, "Development of Air-Entrained, High-Strength Concrete: Mechanical Properties and Resistance to Freezing and Thawing," *Proceedings, CSCE/CANMET International Workshop on*

Concrete for Offshore Structures; St. John's, Newfoundland, Canada, September 1986, 23 p., Available from CANMET, Energy, Mines and Resources, Ottawa, Canada.

[15] M. Pigeon, R. Gange, and C. Fay, "Critical Air-void Spacing Factors for Low Water-cement Ratio Concretes With and Without Condensed Silica Fume," *Cement and Concrete Research*, Vol. 17, 1987, pp. 896-906.

[16] O. E. Gjorv, T. Baerland, and H. R. Ronning, "High-Strength Concrete for High way Pavements and Bridge Decks," *Proceedings, Utilization of High-Strength Concrete,* Stavanger, Norway, 1987, pp. 111-122.

[17] A. Talbot, "Reinforced Concrete Wall Footings and Column Footings," *Bulletin No. 67,* University of Illinois, Engineering Experiment Station, Mar. 1913.

[18] O. Graf, "Strength Tests of Thick Reinforced Concrete Slabs Supported on All Sides Under Concentrated Loads," *Deutscher Ausschuss fur Eisenbeton,* No. 88, Berlin, Germany, 1938.

[19] C. Forsell and A. Holemberg, "Concentrated Loads on Concrete Slabs," *Betong,* Vol. 31, No. 2, Stockholm, Sweden, Feb. 1946, pp. 95-123.

[20] E. Hognestad, "Shearing Strength of Reinforced Concrete Column Footings," *Journal of the American Concrete Institute*, Vol. 50, No. 3, Nov. 1953, pp. 189-208.

[21] F. E. Richart, "Reinforced Concrete Wall and Column Footings," *Journal of the American Concrete Institute*, Vol. 45, Nos. 2 and 3, Oct., Nov., 1948, pp. 97-127 and 237-260.

[22] R. C. Elstner and E. Hognestad, "An Investigation of Reinforced Concrete Slabs Failing in Shear," University of Illinois, Department of Theoretical and Applied Mechanics, 1953.

[23] F. E. Richart and R. W. Kluge, "Tests of Reinforced Slabs Subjected to Concentrated Loads," *Bulletin 314,* University of Illinois, Engineering Experiment Station, 1939.

[24] R. C. Elstner and E. Hognestad, "Shearing Strength of Reinforced Concrete Slabs," *Journal of the American Concrete Institute,* Vol. 53, No. 1, July 1956, pp. 29-58.

[25] J. Moe, "Shearing Strength of Reinforced Concrete Slabs and Footings Under Concentrated Loads," *Development Department Bulletin D47,* Portland Cement Association, Skokie, April 1961.

[26] ACI-ASCE Committee 316, "Shear and Diagonal Tension," *Proceedings,* American Concrete Institute, Vol. 59, Jan., Feb., and Mar. 1962, pp. 1-30, 277-334 and 353-396.

[27] S. Kinnunen and H. Nylander, "Punching of Concrete Slabs Without Shear Reinforcement," *Transactions No. 158,* Royal Institute of Technology, Stockholm, Sweden, 1960.

[28] S. Kinnunen, "Punching of Concrete Slabs with Two-way Reinforcement," *Transactions No. 198,* Royal Institute of Technology, Stockholm, Sweden, 1963

[29] A. E. Long, "Punching Failure of Reinforced Concrete Slabs," *Ph.D. thesis*, Queen's University at Belfast, Northern Ireland, 1967.

[30] H. Reimann, "Zur Bemessung von Dünnen Plattendecken auf Stützen Ohne Kopf gegen Durchstanzen" ("Method for Calculating the Punching Load of Flat Slabs Supported by Columns without Capitals"), *Dr. -Ing. thesis*, Technischen Hochschule, Stuttgart, Germany, Jan. 1963.

[31] A. Long and D. Bond, "Punching Failure of Reinforced Concrete Slabs," *Proceedings of the Institute of Civil Engineers*, Vol. 37, May 1967, pp. 109-136. Discussion: Proceedings of the Institution of Civil Engineers, Vol. 39, June 1968, pp. 151-164.

[32] D. M. Masterson and A. E. Long, "The Punching Strength of Slabs, A Flexural Approach Using Finite Elements," *SP 42 Shear in Reinforced Concrete*, American Concrete Institute, Detroit, 1974, pp. 747-768.

[33] A. E. Long, "A Two-Phase Approach to the Prediction of the Punching Strength of Slabs," *Journal of the American Concrete Institute*, Vol. 72, No. 2, February 1975, pp. 37-47.

[34] A. E. Long, "Predicting the Punching Strength of Conventional Slab Column Connections," *Proceedings of the Institution of Civil Engineering*, Vol. 82, April 1987, pp. 327-346.

[35] H. Gesund and O. P. Dikshit, "Yield Line Analysis of the Punching Problem at Slab/Column Intersections," *SP-30, Cracking, Deflection and Ultimate Load*

of Concrete Slab Systems, American Concrete Institute, Detroit, 1971, pp. 177-202.

[36] H. Gesund and Y. P. Kaushik, "Yield Line Analysis of the Punching Failures in Slabs," *Publications, International Association for Bridge and Structural Engineering*, Zurich, Switzerland, Vol. 30-1, 1970.

[37] M. P. Nielson, M. W. Baresturp, B. C. Jensen, and F. Bach, "Concrete Elasticity - Beam Shear - Punching Shear - Shear in Joints," *Danish Society for Structural Science and Engineering*, Oct. 1978.

[38] H. Andrä, "On the Strengths of Support Regions of Flat Slabs, (Zur Tragverhalten des Auflagerbereichs von Flachdecken)", *Ph.D. thesis*, University of Stuttgart, Stuttgart, 1982.

[39] I. A. Shehata, "Theory of Punching in Concrete Slabs," *Ph.D. thesis*, Polytechnic of Central London, London, 1985.

[40] I. M. Shehata and P. Regan, "Punching in R.C. Slabs," *ASCE, Journal of the Structural Division*, Vol. 115, No. 7, August 1989, pp. 1726-1740.

[41] S. D. Alexander and S. H. Simmonds, "Ultimate Strength of Slab-Column Connections," *American Concrete Institute Structural Journal*, Vol. 184, No. 3, 1987, pp. 255-261.

[42] R. L. Carrasquillo, "Production of High Strength Pastes, Mortars, and Concretes," *Proceedings, Materials Research Society*, Vol. 42, 1985, pp. 151-168.

[43] ACI Comm. tte 363, "State-of-the-Art Report on High-Strength Concrete," *Journal of the American Concrete Institute*, July-August 1984.

[44] R .L. Blick, "Some Factors Influencing High-Strength Concrete," *Modern Concrete*, Vo`. 36, No. 12, Apr. 1973, pp. 38-41.

[45] R. L. Carrasquillo, A. H. Nilson, and F. O. Slate, "Properties of High Strength Concrete Subject to Short-Term Loads," ACI Journal, *Proceedings*, V. 78, No. 3, May-June 1981, pp. 171-178.

[46] K. W. Nasser and H. M. Marzouk,"Properties of Mass Concrete Containing Fly Ash at High Temperatures". ACI Journal, *Proceedings*, V. 76, No. 4, April 1979. pp. 537-550.

[47] A. M. Neville, *Properties of Concrete*, Pitman Publishing Ltd., Second Edition, 1973.

[48] ACI Committee 318 "Building Code Requirements for Reinforced Concrete (ACI 318-83),"American Concrete Institute, Detroit, MI., 1983, 111 p.

[49] " Code for the Design of Concrete Structures for Buildings," (CAN3-A23.3-M84), Canadian Standards Association, Rexdale, ON, 1984, 281 p.

[50] "Structural Use of Concrete: Part1, Code of Practice for Design and Construction," (BS 8110: Part1:1985), British Standards Institute, London, U.K., 1985, 126 p.

[51] P. Regan, "Design for Punching Shear," *The Structural Engineer*, Vol. 52, No. 6, 1974, London, U.K., pp. 197-207,

[52] "Code of Practice for the Structural Use of Concrete," (CP 110: part 1:1972), British Standards Institution London, U.K., 1972.

[53] S. Kinnunen, H. Nylander, and P. Tolf, "Investigations on Punching at The Division of Building Statics and Structural Engineering," *Nordisk Betong*, No. 3, 1978, pp. 25-27.

Appendix A

Chemical and Physical Analysis of Portland Cement and Supplementary Cementitious Materials

Table A.1: Chemical analysis of portland cement and supplementary cementitious
materials

Description of Test	CSA Type 10 *Cement	Fly Ash	Silica Fume
Chemical Analysis, %			
SiO_2	20.20	44.93	95.41
Al_2O_3	5.90	27.79	1.09
Fe_2O_3	2.20	19.06	0.00
CaO	62.80	0.92	0.32
MgO	1.40	1.44	0.73
Na_2O	0.10	0.82	-
K_2O	1.26	0.54	0.61
SO_3	4.0	0.43	0.24
Mn_2O_3	-	0.67	-
Loss of Ignition	2.10	2.88	1.80
Total	100.0	99.48	99.20
$SiO_2 + Al_2O_3 + Fe_2O_3$	-	91.80	-
Potential Compound Composition, %			
C_4AF	8.70		
C_3A	6.90		
C_3S	49.00		
C_2S	22.70		
$C_3S + C_2S$	71.70		

*As manufactured in Newfoundland

Table A.2: Physical analysis of portland cement and supplementary cementitious materials

Description of Test	CSA Type 10 *Cement	Fly Ash	Silica Fume
Physical Tests - General			
Time of set (Vicat Needle, min.)			
Initial	115.0		
Final	220.0		
Fineness: -45 μm	81.7		
Blaine Surface Area m^2/kg	376.0		
% retained on 45 μm by wet sieving		14.5	
Fineness			$20,000 m^2/kg$
Water Requirement, %		92.0	139
Pozzolanic Activity Index with :			
Portland Cement at 28-d, %		99.0	119.1
Lime, MPa		6.7	12.5
Physical Tests - Mortar Compressive strength, MPa			
3-d	28.0		
7-d	32.2		
28-d	37.3		

*As manufactured in Newfoundland

Appendix B

Comparison of Theoretical Results with Others' Test Results

144

Table B.1: Comparison of theoretical results with Elstner and Hognestad's test results

Authors	Slab no.	d, mm	Column size, mm	r_3, mm	ρ, %	f'_c, MPa	f_y, MPa	$\frac{P^1_{calc}}{P_{test}}$	$\frac{P^2_{calc}}{P_{test}}$	$\frac{P^3_{cn}}{P_{test}}$
Elstner	A-1a	117	254	1780	1.15	14.1	332	1.05	0.90	0.96
and	A-1b	"	"	"	"	25.2	"	1.00	0.92	0.97
Hognestad	A-1c	"	"	"	"	29.0	"	1.06	0.98	1.01
	A-1d	"	"	"	"	36.8	"	1.13	1.03	1.03
	A-1e	"	"	"	"	20.2	"	0.98	0.89	0.94
	A-2a	114	"	"	2.47	13.7	321	1.17	1.07	1.15
	A-2b	"	"	"	"	19.5	"	1.10	1.05	1.11
	A-2c	114	"	"	"	37.5	"	1.20	1.19	1.25
	A-7b	"	"	"	"	28.0	"	0.98	0.96	1.03
	A-3a	"	"	"	3.7	12.8	"	1.20	1.13	1.21
	A-3b	"	"	"	"	22.6	"	1.18	1.23	1.19
	A-3c	"	"	"	"	26.6	"	1.05	1.10	1.14
	A-3d	114	"	"	"	34.6	"	1.14	1.20	1.24
	A-4	117	356	"	1.15	26.2	"	1.13	0.94	0.94
	A-5	114	"	"	2.47	27.8	"	1.27	1.07	1.22
	B-9	114	254	"	2.00	43.9	341	1.09	1.06	1.11
	B-11	114	"	"	3.00	13.5	408	1.25	1.25	1.23
	B-14	114	"	"	3.00	50.5	325	1.17	1.20	1.14

Table B.2: Comparison of theoretical results with Kinnunen and Nylander's test results

Authors	Slab no.	d, mm	Column size, mm	r_3, mm	ρ, %	f'_c, MPa	f_y, MPa	$\frac{P^1_{calc}}{P_{test}}$	$\frac{P^2_{calc}}{P_{test}}$	$\frac{P^3_{calc}}{P_{test}}$
Kinnunen	5	117	ϕ 150	ϕ 1710	0.80	27.8	441	1.00	0.97	0.75
and	6	118	ϕ 150	ϕ 1710	0.79	27.2	454	0.95	0.92	0.70
Nylander	24	128	ϕ 300	ϕ 1710	1.01	27.4	455	0.93	0.99	0.99
	25	124	ϕ 300	ϕ 1710	1.04	26.0	451	0.92	0.96	0.99
	32	123	ϕ 300	ϕ 1710	0.49	27.3	448	0.96	0.89	0.90
	33	125	ϕ 300	ϕ 1710	0.48	27.6	462	0.99	0.93	0.93

Table B.3: Comparison of theoretical results with Kinnunen, Nylander and Tolf's test results

Authors	Slab no.	d, mm	Column size, mm	r_3, mm	ρ, %	f'_c, MPa	f_y, MPa	$\frac{P^1_{calc}}{P_{test}}$	$\frac{P^2_{calc}}{P_{test}}$	$\frac{P^3_{calc}}{P_{test}}$
Kinnunen,	b-1	100	ϕ 125	ϕ 1200	0.80	29.6	706	1.13	1.29	1.07
Nylander	b-3	99	ϕ 125	ϕ 1200	0.81	23.7	701	1.15	1.32	1.10
and	b-5	200	ϕ 250	ϕ 2400	0.80	25.2	657	1.47	1.49	1.28
Tolf	b-6	199	ϕ 250	ϕ 2400	0.80	23.7	670	1.43	1.47	1.27
	b-13	98	ϕ 125	ϕ 1200	0.35	27.6	720	1.06	1.04	0.90
	b-14	99	ϕ 125	ϕ 1200	0.34	26.1	712	1.03	1.00	0.89
	b-17	200	ϕ 250	ϕ 2400	0.34	26.7	668	1.18	1.04	1.00
	b-18	197	ϕ 250	ϕ 2400	0.35	25.1	664	1.27	1.13	1.02

$f'_c = 0.83 f_{cube}$
[1] Kinnunen and Nylander (1960)
[2] Shehata and Regan (1989)
[3] Proposed model (1990)